Comput Visual Sci 5: 215–239 (2003)
Digital Object Identifier (DOI) 10.1007/s00791-003-0101-4

Computing and Visualization in Science

Regular article

Mathematical models and numerical methods for the forward problem in cardiac electrophysiology

G.T. Lines[1,2], M.L. Buist[3], P. Grøttum[2], A.J. Pullan[3], J. Sundnes[1,2], A. Tveito[1,2]

[1] Simula Research Laboratory, P.O. Box 134, N-1325 Lysaker, Norway
[2] Department of Informatics, University of Oslo, P.O. Box 1080, N-0316 Oslo, Norway
[3] The Bioengineering Institute, The University of Auckland, Private Bag 92019, Auckland, New Zealand

Received: 21 December 2000 / Accepted: 29 June 2002
Published online: 10 April 2003 –

Communicated by: G. Wittum

Abstract. The purpose of this article is to give an overview of the forward problem of cardiac electrophysiology. The relevant models are derived and the mathematical problem formulated. Different solution strategies are discussed. In particular, the error introduced by solving the equations decoupled is demonstrated. Some novel techniques to deal with this problem are presented.

1 Introduction

The forward problem of cardiac electrophysiology can be summarized as the study of the electrical activity of the heart, from cellular level activity to the non-invasive recording of this activity at the body surface. The article focuses on this problem from a modeling point of view, and justification for the modeling approach to this problem is given below. An overview of different solution techniques is subsequently presented, with particular emphasis on two recently developed approaches [15, 111]. Despite the conceptual simplicity of the problem, the task is far from trivial, and to date we still cannot consider this problem to be solved in any true meaning of the word.

1.1 The electrocardiogram

The electrical activity of the heart can be measured on the body surface and gives a non-invasive representation of cardiac electrical function. This was first demonstrated by Waller more than 100 years ago [123]. His famous demonstrations involved his dog Jimmie standing in buckets of salt solution (the electrodes) which were connected to a recording device involving a column of mercury that was seen to pulsate in time with Jimmie's heartbeat [125]. Such a demonstration was witnessed by Einthoven, who went on to extend and refine the procedure, eventually being awarded a Noble prize for his work in 1924. Einthoven developed an improved device to record the body surface potentials, (the string galvanometer) and defined the concept of P, QRS and T waves, as well as the concept of a heart vector. His first recording machine was large and cumbersome, weighing around 600 pounds and requiring 5 operators [23]. Both Waller and Einthoven put forward evidence to support the idea that the potentials measured on the body surface were the result of cardiac activity and Waller was the first to call such recordings electrocardiograms or ECGs.

The subsequent years saw the development of the first commercial ECG recording machines. As the usefulness of this non-invasive measurement of cardiac electrical activity became widely known and accepted, standards were developed to allow the consistent recording and display of the body surface ECGs. This firstly began with the development of the limb leads (using Einthoven's original notation I, II and III). Wilson [128] introduced the concept of an independent reference (the Wilson central terminal) and his group defined the six precordial leads (V1 to V6) that are included in the standard lead set [56]. Three further leads were developed by Goldberger [33] through modifications to the Wilson central terminal resulting in the augmented limb leads aVR, aVL and aVF. This set of leads which was finally standardized in 1943 comprises the so-called 12 lead ECG which is still the most used procedure in electrocardiography. Originally the ECG was interpreted manually by the measurement of amplitudes and time intervals. The measurements were related to known clinical conditions such as myocardial ischemia, infarction and hypertrophy, and complex sets of diagnostic criteria were developed. During the last 20 years these criteria have been refined and implemented in off-the-shelf computerized ECG recording and interpretation systems.

Waller and Einthoven suggested that the electrical activity of the heart could be represented by a dipole and that the lead recordings were projections of this dipole onto the lead axis. Einthoven's equilateral triangle of leads I, II and III provided a theoretical basis for reconstructing two-dimensional cardiac activity in the frontal plane, see Fig. 1. However, already in 1946 this theory was disputed and several investigators set out to improve the lead system and provide methods for a true spatial reconstruction of the cardiac vector. This concept of an orthogonal or orthonormal lead system is closely linked to that of vectorcardiography, the depiction of the cardiac vec-

Fig. 1. Illustration of an early method of recording the standard limb leads using buckets filled with saline as electrodes. Einthoven's triangle with the lead axis are drawn on the torso. (Lewis [63], copyright Shaw & Sons, London. Reproduced with permission)

tor rotation during the cardiac cycle. The research reached its peak during the 1950s. Tank experiments with artificial torsos and animal experiments were performed to develop the improved lead systems, of which Frank and McFee are best known [26, 68]. However, these lead systems never succeeded in replacing the well established 12 lead system.

Ten years later the notion of a single, rotating cardiac dipole was recognized as inadequate. The attractive idea of summing all electrical activity into a single measure was left and body surface potential mapping, sometimes using hundreds of simultaneous ECG recordings, emerged as a technique to study cardiac activity. Despite demonstrating the clinical utility of some of the information obtained from this large number of recordings [104], body surface potential mapping largely remains in the research environment. Some of the reasons for this probably relate to the difficulty in interpreting such densely sampled ECG data, and the lack of a standard lead set.

Electrocardiographic diagnosis largely relies on morphological descriptions and relatively simple measurements, obtainable by hand. The diagnosis is usually qualitative. As an example, the present criterium for a myocardial infarct is "Any Q wave in leads V1 through V3, Q wave ≥ 30 ms in leads I, II, aVL, V4, V5 or V6. The Q wave changes must be present in any two contiguous leads, and be ≥ 1 mm in depth." [54]. The amplitude measurements are frequently given in mm, not in mV, because of the firmly established paper recorder settings of 1 cm = 1 mV. Relatively few attempts have been made at more complex processing of the body surface ECG. In 1934 Wilson introduced the idea that the integral or net area under the QRST complex, which ideally should be zero, reflected the total excitation of the ventricles and could be used to study local variations in the excitatory process [129]. This measure was termed the ventricular gradient. Despite later refinements, it never gained any practical use. Recent examples of more advanced information processing include the use of spatial QRS- and ST-integrals for quantitative assessment of myocardial ischemia and infarction [99]. However, none of the attempts at more sophisticated signal processing have been able to challenge the traditional way of interpreting the ECG.

With the advent of molecular medicine the causal relationship between changes in cellular processes and manifest disease has become much clearer. Both diagnosis and treatment increasingly focus on the subcellular level. But for a few coarse relationships, e.g. with hyper- and hypokalemia, the possibility of studying subcellular processes through the body surface ECG has so far not been properly exploited.

There are only a few examples where new technology has provided previously unaccessible information from the body surface ECG, e.g. the use of signal averaging to detect and analyze microvolt-level late potentials [103].

The ECG, now close to 60 years old in its present 12-lead form, is the most widely used cardiac diagnostic tool and the most common method of monitoring a person's cardiac activity. There are an estimated 10^6 ECGs performed per day, and the procedure is easily done and inexpensive. For some cardiac conditions the ECG has been replaced by other non-invasive methods, e.g. echocardiography is now the favored method for examining the mechanical function of the heart. However, for assessing myocardial ischemia and infarction, diseases responsible for approximately 20% of the deaths in the Western world, the ECG still remains the primary method. Yet, it is far from perfect, the sensitivity for acute inferior myocardial infarction is barely 60% [71].

Why has a technical system developed with inferior technology remained virtually unchanged during so many years of technical advancement? It is possible that the biological system it is intended to describe is so complicated that the theoretical, experimental and modeling approaches to improve the existing systems and develop new applications have not yet reached sufficient complexity to move the field notably forward. The vast, accumulated empirical knowledge in the form of amplitude and duration criteria related to the old system has maintained its position. A prudent conservatism in the medical profession may also contribute to preserving the present methods.

This introduction does, however, indicate the need both for improvement of present tools and the development of new tools to meet the requirements of modern medicine. The body surface ECG which provides non-invasive, cheap, easily acquired and repeatable information about the heart would in this respect be an ideal tool. With the aid of modern information technology, applications may be tailored to specific needs both in terms of lead systems and signal processing, instead of relying on a common tool for every purpose.

1.2 Why model?

Both Waller and Einthoven used the conceptual model of a dipole to explain the ECG. Later, three-dimensional physical models were employed by Burger [16], Frank [25] and McFee [68] to study the forward problem, i.e. the relationship between cardiac activity and the body surface ECG.

Wilson and Bayley in 1950 made the first very simplified three-dimensional mathematical model of the forward problem which could be handled analytically [130], and in 1964 the first numerically solved model was presented by Gelernter and Swihart [29]. Mathematical modeling in this field is thus not a new phenomenon. However, during the last 20 years the extensive development of numerical methods and computer hardware have made the study of very complex models possible.

Modeling provides a framework within which the building blocks coming from experiments can be placed. This is a common approach in the traditional areas of engineering and physics where many researchers routinely design and analyze complex structures through computer models. This is somewhat due to the solid base of information on material properties and interactions that is available for many traditional building materials. Biological materials and systems are far more complex than human engineered systems and the complex interactions of these systems are correspondingly harder to predict. The physiological process of a heart beat is extremely complicated. It involves many sub-systems and they span several orders of magnitude in the relevant spatial and temporal scales. Spatial scales range from the 1 nm pore diameter of a membrane protein to the 1 m scale of the human body, a range of 9 orders of magnitude. Temporal scales range from 1 μs for Brownian motion to 10^9 s for a human life span, a range of 15 orders of magnitude [52]. It is challenging in itself to understand these sub-systems. To understand how these systems interact to produce the observed large scale behavior is significantly more difficult.

Due to the increasing sophistication in experimental techniques we are continuously increasing our knowledge about the structure and function of the different sub-systems. An obvious example of this is the genome project. From a sequenced gene the structure of the corresponding protein can be found, a prerequisite for understanding how it functions. This type of research has led to an explosion in the amount of information that is available on systems at the smallest scales, to the point where without computer based tools the information would be almost inaccessible.

One argument that is raised against the mathematical models of the problem we deal with here is that they cannot be predictive, meaning that they are only capable of reproducing the experimental results that were used to create them. Presented here are several examples that support the idea that the integrated modeling approach is the way forward.

Evidence already exists that shows computer based models allowing insights into underlying mechanisms in a complex, integrated setting. Rudy [92] presented two examples of this. When looking at mutations of the cardiac sodium channel, a Markovian model of the channel with both normal (wild type) and mutated channels was placed within a cardiac cellular model. This allowed the mechanism of early after depolarizations to be elucidated, through the inactivation and subsequent reactivation of the L-type calcium channel. This would not have been possible using experiments on isolated sodium channels and illustrates the importance of modeling to gain an understanding of the overall picture. The second example cited looks at integration on a larger spatial scale, investigating slow conduction in a cardiac fiber constructed from a string of cardiac cells. Here the conduction was slowed by reducing the conductivity of the gap junctions between the cells and not through a loss of cellular excitability. The use of a mathematical model allowed a quantitative measure of the stability of propagation and produced insights into the mechanisms behind the very slow conduction that can be observed experimentally. Because of the long time taken before a neighboring cell depolarizes, it is actually the L-type calcium channel that provides the charge gradient for propagation to continue long after the inward sodium current has ceased. The above evidence shows that a computer based integrated model was used to demonstrate this mechanism.

The behavior of the whole cannot be understood by simply understanding the behavior of each component. The process is highly nonlinear with very complicated interactions between each of the components which cannot be understood without modeling. Only by performing computer simulations is it possible to aggregate the pieces into a whole and see what consequences an altered component has on the overall system. An example of this is to investigate the effect of a channel blocking drug. The immediate effect is a reduction of flow through that particular channel, but the resulting action potential is not found by simply removing this current. The reason being that other currents are affected by the altered current and the overall result can be counter intuitive. As is the case with the sodium channel example above, a gene defect may result in a malfunctioning channel, and then give rise to macroscopic phenomena such as long QT syndrome.

These examples provide strong evidence that already these models are being used in a predictive manner, not just to reproduce experimental data. Hunter [52] reinforces this by pointing out that governing tissue level equations must obey the physical conservation laws that apply to all materials, such as the conservation of electrical current, mass and momentum. This is another mechanism through which the models can be seen to be predictive and modeling therefore provides additional information that would not be available otherwise. Bassingthwaighte [8] comments on the fact that even though our knowledge of these complex biological systems is very limited, computer based models seem to be the only conceivable alternative to follow up on animal experimentation. Relating back to the earlier questions, one can see that not only is an integrated modeling approach to the forward problem of electrocardiology useful, it is likely to be the only way to deal with the complexity of the problem.

However, the issue still remains that the range of spatial and temporal scales is too large to provide an *exact* model of the physical situation. It is not practical to adopt a traditional top-down or bottom-up approach to these problems. Instead the modeling may be undertaken using a middle-out approach, where the desired spatial and temporal scales are specified and information is gleaned from the scales that lie immediately below those of interest. While this approach may lead to some simplifications, groups of researchers at all levels may then benefit from the advances made at the next level down [8]. Another approach could be to optimize the model for a particular medical problem based on knowledge of the important biological determinants. The fact that under certain circumstances all models can be proved wrong can put modeling of this nature into a negative light. However, that does not mean one should not model, but that one should recognize that all models are to some degree approximations of reality

and one should be aware of the assumptions and approximations when one interprets the outcome of a model.

2 Models

2.1 Models of cardiac electrophysiology

Historically, it has been the top-down approach to modeling cardiac activation that has been to the fore where only the largest level of detail is incorporated as is the case with Einthoven's heart vector [23]. He suggested that the three lead potentials could be viewed as the projections of a vector residing in the heart and moving as if it were in an infinite conducting medium. Further improvements have seen extension from the heart vector, which is essentially a single dipolar source with a fixed center, to multiple moving dipolar and multipolar sources within bounded torso domains. Yet another branch of research in this area uses different types of dipole layer sources. The theory behind these approaches has been around for several decades and although the methods through which these sources are quantified are improving, fundamental problems with this approach are becoming evident. This is mainly due to the lack of detail in these lumped parameter models, the short-comings of which are discussed later in this article.

At the other end of the spectrum, the entire myocardium consists of in the order of 10^{10} cells. When constructing a model of cardiac tissue it is natural to use models of these cells as building blocks and connect them according to the electrical properties between cells. Several groups have used this so-called bottom-up technique [40, 45, 73, 121]. Such an approach can quickly run into problems associated with scale and detail. Furthermore, if large scale phenomenon such as re-entry or body surface ECGs are of primary interest, it is probably not necessary to model each cell. The contribution from any individual cell will be blurred out by its neighbors. A single cell's aberrant activity does not on its own do much – it is the response of a collection of cells that gives rise to collective behavior (for instance a reentrant arrythmia is not the result of a single cell's activity, but rather the collective effect of many cells). Also, farfield effects (such as body surface potentials) do not show the results of a single cell, only a collection. Much of the discrete cellular modeling has, in fact, concluded that on a macroscopic level there is little or no difference between modeling cardiac tissue discretely or as a syncitium [117, 118].

Another modeling option is what has been termed the middle-out approach, in which a model attempts to start between these extremes, and to incorporate both higher and lower level detail when and if needed. This is the option to be preferred here – sufficient detail can be included to significantly extend the concept of a single heart vector and allow more detail to be added at the finer scales when needed and feasible. It also does not suffer the scale and detail problem that one hits early on with a bottom-up approach that is used to model every individual cell, gap junction and ionic process (note that this could also be considered a middle out approach since it starts significantly higher than the level of atoms and genes, although we class it as bottom-up here). Our choice of middle is that of a block of cells – these coming approximately half way in the spread of the length and time scales associated with this problem. Such a block of cells is what is termed a continuum cell, the fundamental building block of the bidomain model.

2.2 The Bidomain Model

Even with the current increases in computational power, it remains infeasible to solve for cardiac electrical activity discretely at a cellular level for all but small preparations of cells. In order to investigate the electrical properties of larger sections of cardiac tissue, a continuum approach may be adopted that averages the electrical properties over a length scale greater than that of a single cell. The continuum approach implemented here is known as the bidomain model and was first proposed by Schmitt [98] before being formulated mathematically by Tung [120]. It has become popular with researchers since its initial formulation and is now used widely to model cardiac electrical activity [42, 50, 74]. The bidomain framework defines a model of cardiac tissue that consists of two interpenetrating domains representing cardiac cells and the space surrounding them. The intracellular domain (subscript i) represents the regions inside the cells and the extracellular domain (subscript e) represents the space between the cells. A third region (or collection of regions) may be included in a bidomain framework that is called an extramyocardial region and is given the subscript o. Where the intracellular and extracellular domains are considered to occupy the same physical space, any extramyocardial regions are defined to be in unique but adjacent physical spaces. The extramyocardial region may be used to model a fluid bath to imitate experimental conditions or to model the torso as is the case in this article. While under normal conditions the extramyocardial region draws current from the cardiac region, this flow may be reversed for example, when a defibrillation shock is applied. The intracellular space is defined to have a potential field ϕ_i and a conductivity tensor σ_i while the extracellular space is defined to have a potential field ϕ_e and a conductivity tensor σ_e, (see Table 1). The derivation of the bidomain equations that is described here is based around the derivation of Henriquez [43]. Some researchers

Table 1. Important symbols in the bidomain formulation. In addition V_m and I_{ion} are defined in H and normal vectors $\boldsymbol{n}$ point outwards from the domain in its subscript. See also Fig. 2

Generic variable names:	Subscripts:
J – current	i intracellular space (H)
ϕ – electrical potential	e extracellular space (H)
σ – conductivity tensor	o extramyocardial space (T)

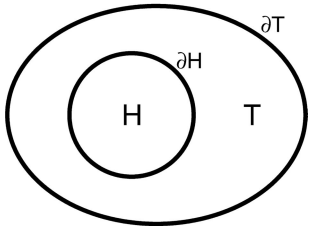

Fig. 2. The bidomain equations are defined on H, the cardiac muscle (excluding cavities), while T is the rest of the body, i.e. $H \cap T = \emptyset$. Note that in general T is not connected due to the ventricular cavities in the heart (not shown)

adopt a slightly different terminology to describe the regions that are used in a bidomain framework. What is termed here as the extramyocardial region is sometimes called the extracellular region and the extracellular region is then called an interstitial region [42].

2.2.1 Bidomain equation derivation. The bidomain equations may be derived in several ways depending on what dependent variables are required. The derivation performed here yields two equations, the first of which is an equation for the extracellular potential. This equation is solved to calculate the extracellular potential field that results from a given transmembrane potential distribution. The second equation is a reaction diffusion equation in terms of the transmembrane potential where the sum of ionic currents from the continuum cells provide the nonlinear reaction term. An alternative derivation yields equations for the intracellular and extracellular potentials but this formulation has the disadvantage that it cannot interface directly with the ionic current models as they are based on transmembrane potentials. The starting definition of the bidomain equations is the definition of the potential difference across the cell membrane which is known as the transmembrane potential and given the symbol V_m, i.e.,

$$V_m = \phi_i - \phi_e \,. \tag{1}$$

It is assumed that the only current flow between the extracellular and extramyocardial space occurs through the boundary conditions imposed on the domains. Ohm's law states that

$$\boldsymbol{J} = \sigma \boldsymbol{E} \,. \tag{2}$$

Here $\boldsymbol{E}$ is the electric field strength, $\boldsymbol{J}$ is a current density and σ is a conductivity. If the quasi-static assumption is used (see Sect. 2.4 for further details) then electric fields can be expressed as a potential gradient, i.e., $\boldsymbol{E} = -\nabla\phi$. Substituting this into (2) gives for the two domains

$$\boldsymbol{J}_i = -\sigma_i \nabla \phi_i \tag{3}$$

$$\boldsymbol{J}_e = -\sigma_e \nabla \phi_e \,. \tag{4}$$

In an isolated case, any current that leaves one domain must cross the cell membrane and flow into the other domain. This requires the change in current density in each of the domains to be equal in magnitude and opposite in sign. The change in current density in each domain must also be equal to the current flow across the membrane.

$$-\nabla \cdot \boldsymbol{J}_i = \nabla \cdot \boldsymbol{J}_e = A_m I_m \tag{5}$$

Here A_m is defined to be the surface to volume ratio of the cell membrane and I_m is the outward transmembrane current density per unit area. By combining (3) and (4) with (5), two equations are generated that represent the conservation of current densities, namely

$$\nabla \cdot (\sigma_i \nabla \phi_i) = A_m I_m \tag{6}$$

$$\nabla \cdot (\sigma_e \nabla \phi_e) = -A_m I_m \,. \tag{7}$$

This implies that

$$\nabla \cdot (\sigma_i \nabla \phi_i) = -\nabla \cdot (\sigma_e \nabla \phi_e) \,. \tag{8}$$

Subtracting $\nabla \cdot (\sigma_i \nabla \phi_e)$ from both sides and using (1), (8) can be rewritten as

$$\nabla \cdot (\sigma_i \nabla V_m) = -\nabla \cdot ((\sigma_i + \sigma_e) \nabla \phi_e) \,. \tag{9}$$

This equation is referred to as the first of the two bidomain equations and is used to solve for the extracellular potential field given a transmembrane potential distribution. The current flow across the membrane, I_m may be described by a time dependent capacitive current and an ionic current

$$I_m = C_m \frac{\partial V_m}{\partial t} + I_{\text{ion}} \tag{10}$$

where C_m is a membrane capacitance per unit area and I_{ion} is the sum of all ionic currents that are calculated from the cellular models. Combining (6), and (10) generates the following equation

$$\nabla \cdot (\sigma_i \nabla \phi_i) = A_m \left(C_m \frac{\partial V_m}{\partial t} + I_{\text{ion}} \right) . \tag{11}$$

In order to convert (11) to have V_m as a dependent variable on the left hand side of the equation, $\nabla \cdot (\sigma_i \nabla \phi_e)$ is added and then subtracted giving

$$\nabla \cdot (\sigma_i \nabla (\phi_i - \phi_e)) + \nabla \cdot (\sigma_i \nabla \phi_e) = A_m \left(C_m \frac{\partial V_m}{\partial t} + I_{\text{ion}} \right) . \tag{12}$$

Using (1), (12) can then be expressed as

$$\nabla \cdot (\sigma_i \nabla V_m) + \nabla \cdot (\sigma_i \nabla \phi_e) = A_m \left(C_m \frac{\partial V_m}{\partial t} + I_{\text{ion}} \right) . \tag{13}$$

Equation (13) is known as the second of the bidomain equations and is used to calculate the transmembrane potential at each time step. It is possible for an external stimulus current to be applied to either the extracellular domain (I_{s1}) or the intracellular domain (I_{s2}) which allows the two bidomain equations to be written as

$$\nabla \cdot ((\sigma_i + \sigma_e) \nabla \phi_e) = -\nabla \cdot (\sigma_i \nabla V_m) + I_{s1} \tag{14}$$

$$\nabla \cdot (\sigma_i \nabla V_m) + \nabla \cdot (\sigma_i \nabla \phi_e) = A_m \left(C_m \frac{\partial V_m}{\partial t} + I_{\text{ion}} \right) - I_{s2} \,. \tag{15}$$

The extracellular domain is sometimes assumed to be highly conducting ($\sigma_e \sim \infty$) or the domains are assumed to be equally anisotropic ($\sigma_i = \lambda \sigma_e$) in an effort to reduce the bidomain equations to a single equation, hence reducing the amount of computational effort required to solve the problem. The simplified equation is known as the monodomain equation and can be written as

$$\nabla \cdot (\sigma \nabla V_m) = A_m \left(C_m \frac{\partial V_m}{\partial t} + I_{\text{ion}} \right) - I_s \tag{16}$$

where the transmembrane potential is equal to the intracellular potential. Here $\sigma = \frac{1}{1+\lambda}\sigma_i$ and $I_s = \frac{1}{1+\lambda} I_{s1} + I_{s2}$. Note that the case $\sigma_e \sim \infty$ is equivalent to $\lambda = 0$. The conductivity values in both the monodomain and bidomain equations are represented at each point in space by a tensor containing

conductivities in the fiber, sheet and cross sheet directions allowing spatially varying fully orthotropic conductivities to be modeled.

2.2.2 Bidomain boundary conditions. There have been some differences in the literature as to what boundary conditions should be applied to the bidomain model [57]. The boundary conditions used here are the original boundary conditions specified by Tung [120] and confirmed by Krassowska [57]. It is assumed that there is no current flow between the intracellular and extramyocardial domains so the boundary condition applied to the domain boundaries in intracellular space is written as

$$(\sigma_i \nabla \phi_i) \cdot n_H = 0\,, \quad x \in \partial H \tag{17}$$

where n_H is a unit vector outwardly normal to the myocardial surface. The ϕ_i parameter is not explicitly represented in the formulation of the bidomain equations so the boundary condition is reformulated (using (1)) in terms of a boundary condition on V_m.

$$(\sigma_i \nabla V_m) \cdot n_H = -(\sigma_i \nabla \phi_e) \cdot n_H\,, \quad x \in \partial H \tag{18}$$

The boundary conditions on the extracellular domain are set up as a current balance between the domain and the surrounding extramyocardial regions

$$(\sigma_e \nabla \phi_e) \cdot n_H = -(\sigma_o \nabla \phi_o) \cdot n_T\,, \quad x \in \partial H\,. \tag{19}$$

The negative sign is used to account for the direction of current flow as both sides of the equation use outward normal vectors. The boundary extracellular potentials are also required to match the boundary extramyocardial potentials, i.e.,

$$\phi_e = \phi_o\,, \quad x \in \partial H\,. \tag{20}$$

In the event that an extramyocardial region is not present, boundary conditions may be applied directly to the extracellular domain to represent the physical problem. In that case, any combination of flux and potential boundary conditions may be applied to the domain boundary, providing at least one potential boundary condition is imposed as this is a prerequisite for obtaining a unique solution.

In a monodomain formulation there is no connection between the intracellular domain and any surrounding media, so the following boundary condition is imposed to prevent current flow out of the myocardial domain.

$$(\sigma \nabla V_m) \cdot n_H = 0\,, \quad x \in \partial H \tag{21}$$

2.2.3 Describing the microstructure. Within the bidomain framework lies the ability to describe the anisotropic nature of the cardiac microstructure through the conductivity tensors. Experimental work has suggested the laminar fibrous structure of the myocardium [58]. The cardiac cells are arranged into fibers and the direction in which the fiber runs gives the first microstructural vector (ν_f). These fibers are then arranged into a branching and anastomosing network of sheets, and the second microstructural direction (ν_s) is given by a vector perpendicular to the fiber axis, in the plane of the sheet. The third axis is calculated through the cross product of the first two axes creating a third vector (ν_c) that is normal to the plane of the sheet. Thus, every point in the myocardium can be assigned a set of orthogonal material axes. The anisotropic electrical properties of the myocardium may then be defined according to this microstructural model with different electrical conductivity values being assigned in each of the three microstructural directions. These tensors enter the model as diagonal tensors representing the tissue conductivity in the fiber, sheet and cross sheet directions. They must then be rotated into the coordinates of the solution domain in order to be inserted into the bidomain equations. A separate tensor is used for both the intracellular and extracellular conductivities, but for a generic tensor σ, the symbol σ^* is used to represent the unrotated tensor, i.e.,

$$\sigma^* = \begin{bmatrix} \sigma_f & 0 & 0 \\ 0 & \sigma_s & 0 \\ 0 & 0 & \sigma_c \end{bmatrix}.$$

Here σ_f is the conductivity in the fiber (ν_f) direction, σ_s is the conductivity in the sheet (ν_s) direction and σ_c is the conductivity in the cross sheet (ν_c) direction. The microstructural axes are described by a tensor quantity, $\dfrac{\partial \nu_j}{\partial x_i}$ that describes the change in material coordinates with respect to the reference coordinate system, x_i. These are known as the direction cosines of the material coordinates and each ν vector represents the direction of an axis in the material coordinate system. The effective conductivity tensor σ is in general not diagonal. The transformation essentially calculates how much of the fiber, sheet and cross sheet vectors lie in each of the global coordinate directions. This rotation is often expressed using matrix products, where if the $\dfrac{\partial \nu_j}{\partial x_i}$ terms are written into a matrix A, then

$$\sigma = A \sigma^* A^T\,. \tag{22}$$

Often the sheet structure is left out of models of the myocardium, where conductivities are only prescribed in the fiber and cross fiber direction creating the situation of transverse anisotropy.

2.3 Models of cardiac cells

In a bidomain context, the aim of a biophysically based cardiac cell model is to represent the electrical activity of a cell by accurately modeling subcellular features such as specialized compartments and ion transfers through channels, pumps and exchangers. The models are usually formulated by fitting equations to experimentally obtained data. The resulting models represent what is believed to be happening in a single cell and may be placed as a continuum cell into the bidomain framework.

The first model of cellular electrical activity was created by Hodgkin and Huxley [44]. The model is based on mathematical representations of different ions flowing across a cell membrane, driven by concentration gradients. In order to describe the time and voltage dependence of an ion channel, Hodgkin and Huxley proposed a model that uses gating variables. The general form of this model is

$$I_x = g_x \cdot (V_m - E_x) \tag{23}$$

where I_x is the current flow through the ion channel x, g_x is the conductance of the channel and E_x is the reversal potential for the channel which is the Nernst potential for the ion or ions. The conductance is the maximal conductance $\overline{g_x}$ multiplied by the state of the channel which is modeled with a set of gating variables. For a channel with m different gates, each with n_i sub-units per gate, the model of the channel conductance is given by

$$g_x = \overline{g_x} \prod_{i=1}^{m} x_i^{n_i} . \tag{24}$$

A generic gating variable x has a time dependence which can be expressed as

$$\frac{dx}{dt} = \alpha_x(V_m) \cdot (1 - x) - \beta_x(V_m) \cdot x \tag{25}$$

or

$$\frac{dx}{dt} = \frac{x_\infty - x}{\tau_x} \tag{26}$$

where

$$\tau_x = \frac{1}{\alpha_x(V_m) + \beta_x(V_m)}$$

$$x_\infty = \frac{\alpha_x(V_m)}{\alpha_x(V_m) + \beta_x(V_m)} .$$

Here x_∞ represents the steady state behavior of the gate. The $\alpha_x(V_m)$ and $\beta_x(V_m)$ coefficients are known as rate constants and are voltage dependent. The rate constants are usually represented by an empirical formula or a set of piecewise empirical formulae. Using this model of an activation channel, the gate is fully open when $x = 1$ allowing maximum current flow and fully closed when $x = 0$ prohibiting any ion transfer. Ion channels often require multiple gates to properly represent the activation and inactivation processes. The action potential from a single cell is generated using the formula

$$\frac{dV_m}{dt} = \frac{-(I_{\text{ion}} + I_s)}{C_m} \tag{27}$$

where I_{ion} is the sum of all the individual ionic currents, I_s is an externally applied stimulus current and C_m is the specific capacitance of the cell membrane. This general form is still used for ion channels in the most complex models around today. The original Hodgkin–Huxley model is based upon three individual ionic currents and was developed using data gathered from giant squid axons. Following this work, many other biophysically based models have been developed, including the models of Beeler–Reuter [9], DiFrancesco–Noble [77], Luo–Rudy [66], and Winslow et al. [131]. For a review of these types of cell models see [79] or [132].

The level of detail in many of these models is continually increasing, much of which probably exceeds current experimental abilities to validate. Which cellular model to use will depend on what questions are posed and the desired application of the results. Often it is not necessary to model the ionic currents of a cell with the accuracy and complexity inherent in the biophysically based models. For subthreshold situations where the membrane does not change permeability even a linear model could be sufficient. With a view to investigating phenomena on a larger spatial and temporal scale, several ionic current models have been developed that do not seek to model subcellular processes but only to provide an action potential at a minimal computational cost. The simplest of these models is a polynomial model that uses just one variable [51]. The next level of refinement introduces the FitzHugh–Nagumo [24, 75] type models which includes a recovery variable in addition to a cubic polynomial depolarization model. With these models the whole cardiac cycle is modeled, not just the depolarization but also the plateau phase and the repolarization of the membrane. Another simplified cardiac cell model was developed by vanCapelle and Durrer [121] who used again used a cubic polynomial depolarization, and a piecewise polynomial recovery process.

2.4 The torso model

The governing equations for the problem of calculating the potential distribution within the torso are Maxwell's equations. These equations may be simplified by what is termed the *quasi-static* assumption [80]. For the range of frequencies over which bioelectric signals are generated, the capacitive, inductive and propagation effects of the body may be ignored leaving the torso to be modeled as a passive volume conductor.

The electric field strength, $\boldsymbol{E}$ may be expressed as the gradient of a scalar potential field, ϕ_o, i.e.,

$$\boldsymbol{E} = -\nabla \phi_o . \tag{28}$$

The total current may be expressed as the sum of the conduction current, $\sigma \boldsymbol{E}$, and any source currents. Thus $\boldsymbol{J}$, the total current, is given by

$$\boldsymbol{J} = \boldsymbol{J}_s + \sigma \boldsymbol{E} \tag{29}$$

where σ is the tissue conductivity and $\boldsymbol{J}_s$ is the sum of any source currents. Because the passive torso does not store charge, the net current flow into and out of a region is zero, hence

$$\nabla \cdot \boldsymbol{J} = \nabla \cdot (\boldsymbol{J}_s + \sigma \boldsymbol{E}) = 0 . \tag{30}$$

This may be written as

$$\nabla \cdot (\sigma_o \nabla \phi_o) = -\nabla \cdot \boldsymbol{J}_s = I_v . \tag{31}$$

Since the conductivity tensor σ is symmetric and positive definite (31) is an elliptic partial differential equation. As there are no sources outside the heart surfaces, the right hand side of (31) may be set to zero leaving a generalized Laplace equation as the governing equation for the passive torso regions.

$$\nabla \cdot (\sigma_o \nabla \phi_o) = 0 \tag{32}$$

In general each torso region will have a different conductivity tensor which is either isotropic or anisotropic depending on the physical properties of the tissue being modeled.

2.4.1 Torso boundary conditions. The boundary conditions applied to the torso mesh are dependent on the medium surrounding the region of interest. Outside the torso surface the air is assumed to have a zero conductivity meaning no current can flow from the torso. This is set up as a zero normal flux boundary condition,

$$(\sigma_o \nabla \phi_o) \cdot n_T = 0\,, \quad x \in \partial T \tag{33}$$

where n_T is now a unit vector outwardly normal to the torso surface. The application of zero flux boundary conditions to the air boundaries of the torso generates solutions that may only be determined to within an arbitrary additive constant. Computationally this causes singular matrix systems. If the solution is computed at n points, the stiffness matrix is $n \times n$ and it will be of rank $n-1$. To overcome this problem a reference potential is set at some point on the torso surface, ϕ_o^{ref}, thus adding an equation. Since the rank is $n-1$ one of the equations in the original system can be removed, thus we end up with an $n-1 \times n-1$ system with full rank.

If, however, all equation are retained there is one more equation than unknowns, which makes a seemingly overdetermined system of equations. An overdetermined matrix system may be solved using a least squares approach to minimize the error in each equation. Alternatively some form of matrix deflation can be used [37], or the consistency criterion proposed by Salu [95]. Computationally the method of Salu appears to be the most efficient. The existence and uniqueness of a solution to (32) with Neumann boundary conditions (33) and the additional requirement that

$$\int_T \phi_o \, dV = 0\,,$$

is given in [22].

For region boundaries inside the torso, such as the lung surfaces which are surrounded by the torso cavity, boundary conditions known as *interface conditions* are applied. The torso surface is the only place where boundary conditions that derive from the physical problem are applied. These interface conditions are the result of discretising the torso into different regions and therefore are not boundary conditions in the physical problem. Across the internal boundaries continuity of both current and potential is maintained. If two regions p and q are adjacent, the two imposed interface conditions are

$$\begin{aligned} &\phi_p = \phi_q \\ &\left(\sigma_p \nabla \phi_p\right) \cdot n_p = -\left(\sigma_q \nabla \phi_q\right) \cdot n_q \end{aligned} \tag{34}$$

where n_p and n_q are unit outward normals from the regions p and q respectively. Note that the boundary conditions between coupled extracellular and the extramyocardial regions (Equations (19)–(20)) may also be thought of as interface conditions.

2.5 Model summary

The equations that govern the forward problem of electrocardiography from a cellular level through to the body surface can now be compiled in the following manner. If the cardiac region is denoted by H and the torso regions by T then

$$\frac{\partial s}{\partial t} = F(t, s, V_m) \quad \text{in } H \tag{35}$$

$$V_m = \phi_i - \phi_e \quad \text{in } H \tag{36}$$

$$\nabla \cdot ((\sigma_i + \sigma_e)\, \nabla \phi_e) = -\nabla \cdot (\sigma_i \nabla V_m) + I_{s1} \quad \text{in } H \tag{37}$$

$$\nabla \cdot (\sigma_i \nabla V_m) + \nabla \cdot (\sigma_i \nabla \phi_e) = A_m \left(C_m \frac{\partial V_m}{\partial t} + I_{\text{ion}} \right) - I_{s2} \quad \text{in } H \tag{38}$$

$$\nabla \cdot (\sigma_o \nabla \phi_o) = 0 \quad \text{in } T \tag{39}$$

and these equations are subject to the following boundary conditions

$$(\sigma_i \nabla V_m) \cdot n_H = -(\sigma_i \nabla \phi_e) \cdot n_H \quad \text{on } \partial H \tag{40}$$

$$(\sigma_e \nabla \phi_e) \cdot n_H = -(\sigma_o \nabla \phi_o) \cdot n_T \quad \text{on } \partial H \tag{41}$$

$$\phi_e = \phi_o \quad \text{on } \partial H \tag{42}$$

$$(\sigma_o \nabla \phi_o) \cdot n_T = 0 \quad \text{on } \partial T \tag{43}$$

Equations (35)–(43) then represent the coupled bidomain/torso problem. In (35) we have introduced the variable s, which is a vector collecting the gate variables and intracellular ionic concentrations occuring in the cell model ODEs. Because the heart tissue is regarded as a continuous medium s is a vector-valued field defined throughout the heart muscle, characterizing the state of the cells in each spatial point.

To get a unique solution of (35)–(43) we demand in addition that

$$\phi_o(x_{\text{ref}}) = 0$$

for some x_{ref} on ∂T.

3 The data problem

In order to fully specify the model given by (35)–(43) the appropriate independent variables have to be defined and specified. These include the intracellular, extracellular and extramyocardial conductivity tensors, which all depend intimately on the structure of the cardiac region and surrounding tissues. One also needs a description of the cellular-level properties used in the ionic current model, and their spatial and temporal variations. Finally, the computational domains H and T must be appropriately described, which incorporates details of the dynamic structures of the heart including atrial and ventricular tissues, and the conduction system of the heart. Further complicating this task is the fact that this information is needed for both normal and diseased states, and on a patient-specific basis.

This is a monstrous task and is currently impossible to achieve. However, significant progress can be made toward defining the geometry and material properties appropriately, and further advances in this area are being continually made. In respect to the ionic current models, there is an unquestionable experimental need to further validate and refine the existing models using human cardiac cells and tissue preparations. Currently many models rely on parameters from different species despite known differences. However, under

certain conditions realistic representations of cardiac action potentials are possible with existing cellular models. More is also being learned of the spatial variation of cellular properties both in-vitro and in vivo, but again much more experimental work is needed.

The heart consists of several distinct cell types with different characteristics, and in the ventricular wall studies have shown that the shape and duration of the cardiac action potential changes transmurally [3, 102].

The conductivity tensors of the heart are closely tied to the underlying structure. Significant effort has been undertaken to accurately measure this structure in canine ventricle through in vitro measurements [58, 76]. More recently measurements have been taken from porcine myocardium at The University of Auckland where a fully automated confocal tissue imaging system is under construction. Improvements in MRI technology also offer hope that structure can be inferred non-invasively through diffusion imaging [7, 27, 48, 87]. Some experimental work has focussed on what the conductivities should be in each of the myocardial directions, but so far the results have been inconsistent [91]. The electrical conductivities are also required for all of the other tissue types within the torso where much of the experimental work has been performed on canines.

In parallel with the proper construction of a model of the myocardium is the problem of modelling the specialized conduction system that governs the activation of the heart. Gathering representative data in this area is definitely a problem. The conduction system is relatively easy to stain experimentally but has been seen to be hugely variable between subjects. One must therefore turn to some sort of statistical or tree growth approach to create a model that represents the actions of the specialized conduction system rather than an anatomical description of the conduction system itself.

At the length scales required for ECG signals of the torso, imaging modalities such as MRI, CT and even ultrasound allow one to obtain sufficient detail from which to construct appropriate representations of the geometry of the torso. Sachse et al. [93] has used the Visible Human Data set [122] to extract detailed 3D models of a large set of internal organs, including cardiac and skeletal muscles with fiber directions. Other researchers who have used fully or semi-automated techniques for torso segmentation include Lorensen [64], Kauppinen [55] and Cordier [21].

4 Solution methodologies

4.1 The problem size

To sufficiently resolve the spatial scale of the dynamics during the depolarization phase a very fine spatial and temporal resolution is required. For realistic cell models the internodal distance should not be greater than 0.2 mm or 50 nodes per cm in each spatial dimension. In 3D this yields $50^3 = 125$ k nodes per cm^3. A typical heart has volume of 250 cm^3 yielding in excess of 31 million computational points for a whole heart simulation.

The memory requirement for such a simulation will be large. The tests shown in Table 2 indicate that in the order of 2 kb of memory is necessary per node. The following analysis gives a break down of this number.

Table 2. The memory requirements (in Mb) for different problem sizes (measured by the number of computational nodes). From the third row we see that the growth is linear in the problem size, with approximately 2 kb per node and offset of 5.87 Mb. The numbers are from a 3D simulation with an isolated heart, i.e. no computational nodes in the torso

Problem size (N)	Memory (M)	$(M-5.87)/N$
125	6.108 Mb	1.9040 kb
729	7.396 Mb	2.0933 kb
4913	15.976 Mb	2.0570 kb
35 937	79.972 Mb	2.0620 kb
274 625	563.000 Mb	2.0287 kb

Each variable will need 8 bytes per node in double precision. A variable is needed for each of the two potentials and also for each of the state variables of the ODE model of the cell membrane and any cellular model parameters that vary spatially throughout the domain. This typically totals in the order of 30 variables and possibly more than 100 parameters as more information is gathered on the regional variations in cellular properties.

The mesh must also be stored in memory. Each mesh point requires three spatial coordinates. In addition the connective structure must be stored. With a finite element approach, the number of elements per node will depend upon the element type. To get some specific numbers we assume tetrahedral elements. In that case six elements per node is a reasonable approximation, the exact number will depend upon the geometry. Each element is represented by four node numbers, each using one integer (4 bytes), so the four numbers will require the memory equivalent of two doubles. The grid will thus require $3(\text{coordinates}) + 2 \cdot 6(\text{elements}) = 15$ doubles per node. Another important contributor is the stiffness matrix. One is needed for each of the two equations in the bidomain model. Using linear, tetrahedral elements we have found that 16 non-zero entries per row is a realistic number. By using a sparse matrix it suffices to store only the entry (8 bytes) and an index (4 bytes). The demand per node then is equivalent to $16 + 8$ doubles. Counting both matrices we need 48 doubles per node. The two right hand sides gives us another two doubles per node. If this is extended to linear cuboid elements then 27 non-zero entries will be present in each row, almost doubling the memory requirements. If a finite difference approach is taken, up to 27 non-zeros will typically be needed for each row of the two matrices, depending on the type of differencing scheme employed. For non-uniform meshes, mapping arrays must be stored to relate the mesh to a normalized space. Therefore, on the order of 60 doubles will be required for each finite difference point, and possibly several integers based on the type of sparsity structure required for a given solution technique.

Another set of information that has a large memory overhead is the 9 doubles required to define the three microstructural axes at each point. Add to this 6 doubles to fill out the two diagonal conductivity tensors and 12 when they are rotated into the effective tensors (from the symmetry of the tensors), and the microstructure requires 27 doubles at each point. A finite difference approach requires the first order derivatives of the conductivity tensors and these are often precalculated.

In summary we find that we could easily need 200 doubles (1600 bytes) or more per mesh point, and thus 50 GB

for a full scale heart simulation. In practice the amount of memory actually used is larger, with many integer arrays needed and book keeping arrays to speed up computations. The numbers could be larger still for efficiency reasons, as often memory can be traded for speed. Added to all this is the need to model the torso as well. The same spatial scale is not needed throughout the torso since detail diminishes with distance. However, near the heart the length scale is still submillimeter. Because of the large size of the torso relative to the heart, it is estimated that a torso mesh at a converged resolution will increase the size of the overall problem by at least 50%.

If one is interested in simulating a full heart beat of 500 ms, then 50 000 time-steps are required with an 0.01 ms time step. Although steps larger than this are often reported in the literature, simulations have shown that this step size is required to generate accurate conduction velocities with the bidomain model.

A typical value for CPU consumption is 1ms per node per time step. Multiplying these numbers give us total CPU time of 50 years for a whole heart, full cycle simulation on a single CPU. To model reentrant phenomena would clearly require many heart beats to be simulated, further increasing the time.

4.2 Common approaches

From the discussion in the previous section it is clear that the problem is very CPU and memory intensive and even with the middle-out modeling approach, still beyond the computing power of all but perhaps the very largest supercomputers (although this situation is improving all the time). In the following we will highlight some of the efforts that various groups have made in dealing with these challenges. Both the isolated bidomain problem where the heart is not connected to any outside tissue, and the coupled problem with a conductive medium outside the heart are considered.

4.2.1 Integration techniques. There are two main types of integration that are required to solve the bidomain equations, the first is the integration of the time derivative that is present in the capacitive component of the transmembrane potential equation (15), and the second is the integration of the system of ordinary differential equations that is used to describe the cellular electrical properties of the continuum cells at each solution point. There exists several way of integrating the bidomain equations ahead in time. Many of these integration techniques fit into the schematic form:

$$\frac{V_m^{n+1} - V_m^n}{\Delta t} = \nabla^2 V_m^p + f(V_m^q) \tag{44}$$

The simplest and therefore most common scheme is forward Euler, $p = q = n$, which does not involve solving systems of equations for the transmembrane solution (a system of equations is still required for the extracellular potential solution). This scheme is only conditionally stable based on the potential gradients, time steps and spatial discretization. On the other extreme is the fully implicit approach, $p = q = n + 1$, here a non-linear set of equations must be solved for each time step, requiring the use of a root finding technique. Larger time steps can be taken, but the cost per step is much larger. A semi-implicit approach, $p = n + 1$, $q = n$ is a popular compromise. Here only linear equations must be solved but large time steps are still possible. A variant is the Crank–Nicholson scheme $p = n + 1/2$, i.e. $\nabla^2 V_m^p = (\nabla^2 V_m^n + \nabla^2 V_m^{n+1})/2$. With $q = n$ this is not a second order accurate method in time, but probably more accurate than the semi-implicit method.

More sophisticated techniques have been proposed that do not fit into the structure in (44). For example, Skouibine et al [106] makes use of a predictor-corrector technique and they report performance that is superior to a standard explicit Euler approach. The operator splitting method of Qu and Garfinkel [84] is covered later in the section on adaptive algorithms, and is not on the form given in (44).

The second type of integration that deals with the integration of the cellular ionic currents is perhaps best customized to the ionic current model that is being integrated. Simple cell models, especially those that are not biophysically based, may only require a simple Euler or Runge-Kutta scheme. More complicated models may require more advanced integrators such as an Adams–Moulton technique with adaptive polynomial orders and time steps [101]. As the cell models become more complicated, incorporating features over a wider range of scales, the systems are becoming more stiff and so the method of Gear [28] may be favored.

It has been found that for the Noble 98 cell model [78] a time step of no greater than 0.01 ms is required to generate accurate conduction velocities. A Gear based method is able to integrate this cell model with a time step of 0.1 ms but using steps this large introduces significant conduction delays. The simple Euler integrator is able to integrate the model at the 0.01 ms time step required for accurate conduction and is computationally much faster than the Gear method because of its simplicity. There is no discernible difference between the cellular time courses between the two integrators when both use the 0.01 ms time step so in this case using the Euler integrator is highly desirable.

4.2.2 Adaptivity. The strict demands on spatial and temporal resolution are caused by the fast dynamics of the wavefront. Away from the wavefront the demands are less strict and this fact can be utilized to construct adaptive algorithms. Some care must be taken with this approach however. For example in the cellular model developed by Jafri, Rice and Winslow [53], it appears that it is the intracellular calcium spike in the diadic space (the space between the sarcolemma and sarcoplasmic reticulum) that limits the time step, and this spike is not at, or relatively near the wavefront.

A simple method is to use explicit time steps and divide the tissue into an active and a passive part. Only variables within the active region are updated [4, 41, 82]. This approach has been found to cause distortions in the action potential. Also, the quality of the solution is questionable when performing reentry simulations with head-tail interaction [85].

Quan et al. [85] suggested an algorithm where the time step can vary locally. The computational domain was divided into a pre-specified set of subdomains, and the time step of each domain was controlled only by the nodes inside the domain. This allows for passive regions to take longer time steps, and small time steps are only applied in domains with active nodes. To reduce round off errors the local forward

Euler steps are intertwined with small, global implicit steps. The reported speed-up was a factor of 3–17, depending on the number of domains and the problem size.

Qu and Garfinkel [84] and also Lesh et al. [62] use operator splitting to achieve spatially varying time steps. The diffusive and non-diffusive part associated with the ionic currents are solved in different steps. Adaptive time stepping is then used on the non-diffusive part. Since there is no communication between neighboring nodes in this part of the problem, the time step can vary locally as the dynamics dictate.

Cherry et al. [17] suggested a scheme where both the spatial and temporal resolution varies. They report a factor of 5 reduction of the computational effort compared to an explicit forward Euler scheme with full resolution. The degradation in error is between 1% and 6%.

4.2.3 Parallel algorithms. Parallel hardware has been employed by several groups. There are several possible ways of implementing a parallel simulator. The different ways can be arranged according to the level at which the parallelization takes place. At the lowest level the parallelization is done by the compiler (loop-level parallelization). Such strategies are seldom efficient. Parallelization at the linear algebra level is another possibility. Here the parallelization is done by segmenting the vectors and matrices of the computation such that vector addition, inner products and other basic operations can be computed with little inter-processor comunication.

The highest level of parallelization is to have individual simulators running on their own processors, assigned to a specific geometric sub domain. Generally speaking higher levels of parallelization require less frequent communication making it more attractive on platforms with a high latency network.

Saleheen and Ng [94] have implemented a finite difference scheme which utilizes a low level form of parallelization. They report good efficiency although no speed-up numbers are given.

An example of high level parallelism is given by Porras et al. [83]. They use a set workstations connected by a high latency network. Only subproblems are tackled, either parts of the ODE problem or the linear equation system, thus the theoretical speed-up is low. The speed-up is good on the computation of ion currents, but poor for the conjugate gradient iterations. This is as expected since there is a smaller amount of calculation per required communication step compared to ion current calculations which are spatially decoupled.

4.2.4 Decoupled approaches. A lot of CPU work can be saved by altering the mathematical formulation of the problem in different ways. We group these techniques here under the heading decoupled approaches.

Previous methods of generating body surface potentials from an active cardiac region mostly utilize some form of equivalent cardiac source that is applied to the cardiac region within a passive torso. Many examples of this approach may be found in the literature [31, 35, 49, 126, 127]. Often with this approach, the feedback loop that allows the torso to influence the active cardiac region is neglected as the generation of the cardiac source and its application to the torso are performed in two separate steps. Another problem with this two step approach is that the current flowing across the epicardial and endocardial surfaces from the equivalent cardiac source may not be consistent with the current flow from a detailed cardiac model. These factors that do not ensure there is current conservation detract from the accuracy of the torso solutions.

Einthoven [23] developed the first mathematical model of cardiac electrical function. The electrical output of the heart was lumped into a heart vector that was projected onto the faces of an equilateral triangle whose vertices consisted of one leg and two arm electrodes. The heart vector was later expressed as a dipole source by Wilson [128] who suggested a positive pole could be placed immediately in front of the activation wave with a negative pole immediately behind the wavefront. A dipole source based approach is still often used today as a simple lumped parameter way of describing the electrical activity of the heart. Evidence is presented here, however, that suggests a dipole source representation may be an inadequate approximation. As early as 1963, experimental observations by Taccardi [112] suggested that a multipole instead of single dipole cardiac source may be required to account for some of the more complex waveforms. Barr [5] described the calculation of body surface potentials from a given dipolar cardiac source in an irregular torso geometry, based on a boundary integral formulation which is essentially equivalent to a zeroth-order boundary element method. This was followed by some of the early modeling investigations into the effects of both the ventricular blood mass and torso inhomogeneities on recorded potentials in a concentric spheres system [69, 70]. Here the thickness of a homogeneous muscle layer was adjusted to reflect the inhomogeneous nature of the skeletal muscle tissue.

Often dipole sources are formulated to reproduce an experimentally recorded activation pattern. Bradley [13] used a single moving dipole source that had been fitted using a least squares approach in order to reproduce a measured electrocardiogram. Others use a multiple dipole approach, Miller [72] divided the heart into 23 regions, each of which contained a single dipole. These dipole models produce a lumped or integrated representation of the distributed cardiac activity. Researchers also use dipole sources to examine the effects of myocardial anisotropy [86, 113], the effects of torso inhomogeneities [13] or a combination of the two [97]. The formulation of several different types of dipole source models are given in Gulrajani [35].

Barr [6] adopted a different approach to transfer potentials from the heart to the body surface. By creating a matrix of transfer coefficients based on the geometry of the heart/torso system, a given set of epicardial potentials could then be transferred to the body surface through a matrix–vector product instead of a complete solution process. This approach has also been used more recently by Shahidi [100] who used a transfer coefficient approach with a three dimensional finite element torso model and recorded epicardial potentials. This approach does require the epicardial potentials to be known.

Another class of cardiac models, termed empirical models, seek to create a stylized representation of cardiac activation. These models do not attempt to recreate the underlying electrophysiology of cardiac tissue, which ultimately limits their applications, but in general they may be solved quickly because of their simplifications. One such approach is cellular automata modeling where the cardiac domain is discretized into regular elements, each representing a small tissue unit. These blocks of tissue may be in a finite number of states

where rules are set up to govern the transitions between the states along with rules prescribing the activation time of a tissue block relative to its neighbors. Cellular automata models have an advantage over other empirical models in that they can have rules regarding tissue recovery, allowing the modeling of some reentrant phenomena. While these models have been popular in large scale simulations, the rule based system can not model any phenomena that change cellular properties over the space of multiple beats, such as the formulation of an infarct. They are also unable to cope with externally applied defibrillation shocks. Overviews of the history of cellular automata modeling may be found in Sands [96] and Rogers [88].

A different empirical approach uses a constant wave speed model and is known as the Huygen's wavefront method. The cardiac region is discretized into a regular arrangement of cells over which the position of the wavefront is calculated at each time step. The Huygen's wavefront method uses a governing equation of the form

$$|\nabla u| = 1 \tag{45}$$

where u represents an activation time. This formulation generates ellipsoidal isochrones where $u = constant$ defines an activation wavefront. For a given active cell, each inactive neighboring cell is considered active after a fixed time interval. Hookings [46] developed a Huygen's wavefront framework that incorporates fiber rotations in two and three dimensions, including an anatomically based ventricular geometry. More recently Adams [1] employed a Huygen's wavefront approach over a realistic ventricular domain. A review of this type of model is given in Plonsey [81]. The main disadvantage of this approach is that only the upstroke of the activation wave is modeled so the investigation of reentrant phenomena is not possible. In addition to this, propagation is restricted to occur in a finite number of directions meaning that wavefront curvature has no effect on the speed of propagation. Using an eikonal equation to calculate the position of the wavefront overcomes this problem. Whereas the Huygen's wavefront method uses a parabolic equation, the eikonal approach uses an elliptic equation and the wavefront position at all times can therefore be calculated in one step.

The governing eikonal equation has the form

$$|\nabla u| = 1 + \nabla^2 u \tag{46}$$

where the inclusion of the diffusive term allows the wavefront curvature to influence the wave speed. Applications of the eikonal approach include a simplified three dimensional model of the left ventricle that was solved using finite elements [19, 20]. Tomlinson [115] used a finite element method to solve an eikonal equation over a realistic ventricular geometry. The final model required only 180 tricubic Hermite elements to describe the wavefront position.

Numerous authors have adopted a continuum bidomain (or monodomain) framework to model different aspects of cardiac activation. Street [109] used a bidomain framework with a modified FitzHugh–Nagumo ionic current model to investigate propagation across a region containing connective tissue. Geselowitz [32] used a bidomain framework to model propagation in a thin tissue layer. Cimponeriu [18] used a finite difference technique with a monodomain model on a grid of 200×200 cells. By adjusting the parameters in the Luo–Rudy cellular model [66] they investigated different cardiac disease states and created theoretical ECGs based on a dipole source within an infinite volume conductor. A series of papers has also been written describing the activation of a monodomain model of a simplified left ventricle where the cells use a cellular automata approach [59–61]. The finite difference method was again used to calculate diffusion and the extracellular potential fields were calculated though equivalent cardiac dipoles. Other authors [47, 90] have used a bidomain framework to investigate the effects of including a fibrous cardiac microstructural model. A large volume of research focuses on using the bidomain model to investigate the effects of defibrillation shocks [50, 105, 119]. Most bidomain implementations are based around a finite difference solution technique but the finite element method has also been used [89], as has the finite volume technique [38, 39]. Summaries of the bidomain framework are available in Henriquez [43] and Plonsey [81].

Most torso models utilize some form of boundary element technique to define the torso surface on which potentials are calculated. An example of this is seen in Stanley [107] who used a boundary integral technique. Their framework was later extended to include a coupled finite element/boundary element model through what was termed the *combination method* [108]. This framework, however, only used low order elements and had very simple coupling between the methods. Bradley [12] used a coupled finite element/boundary element technique to model a human male torso. High order elements and a general coupling strategy were used throughout the torso to ensure derivative continuity and to reduce the number of elements needed for a converged solution. Kauppinen [55] differed from this standard approach and used a finite difference technique to evaluate potentials within the torso that result from a simple dipole source. Automatic medical image segmentation was used to create detailed torso models to specific geometries.

Berenfeld [10] created a cardiac model from 145 000 cubes and used a finite difference technique along with FitzHugh–Nagumo cellular model variations [24, 75] to model cardiac electrical activity. This was later extended to 215 000 cubes [11] and included the addition of a specialized ventricular conduction system. Body surface potentials were then generated in a second step by calculating a single dipole source and evaluating the potentials at appropriate sites in a homogeneous, unbounded torso model.

Four studies have been found that investigate the calculation of body surface potentials from cardiac cells using equivalent cardiac sources and proper bounded torso models. Wei [126] used approximately 50 000 connected elements to model the cardiac geometry and a cellular automata model was used to activate the cardiac tissue that was categorized into 16 cell types. The myocardium was divided into 27 ventricular and 27 atrial regions, and equivalent dipole sources were calculated within each region through the summation of cellular dipoles. These dipole sources were then used to calculate body surface potentials. Weixue [127] constructed a 65 000 element heart model from computer tomography (CT) images with a cubic close-packed structure. Again a rule based cellular automata approach was used to model the cardiac activation. Cellular dipoles were created based on the transmembrane potential gradient and were summed to cre-

ate 82 cardiac dipoles. The dipoles were then placed inside a triangulated torso mesh to generate body surface potentials. Huiskamp [49] created a model of the ventricles that was composed of 810 546 elements and used a biophysically based membrane model in a monodomain framework to simulate the spread of excitation. A double layer cardiac source was then defined on the endocardial and epicardial surfaces assuming an equal anisotropy ratio, and the boundary element method was used to solve for the torso surface potentials. In the most recent study of this nature, Gulrajani [36] created a cardiac model from 12 million solution points with a Luo–Rudy [65] cellular model. Here an equal anisotropy assumption was used to simplify the system to a monodomain model, and the computations were performed on a large parallel shared memory computer. From the cardiac solution, 58 time varying current dipoles were calculated and these were placed inside a torso model to calculate body surface potentials.

4.3 Experimental results

The physical situation suggests that a fully coupled approach is the appropriate means of solving the forward problem as boundary conditions are only present on the surface of the torso. As early as the 1960's, researchers began questioning the validity of the classic heart vector approach when experimental observations suggested that a dipolar cardiac source was not sufficient to account for some of the more complex waveforms observed on the body surface. A higher order multipolar source was then suggested as an alternative [30, 112]. More recent experimental evidence has elucidated the inadequacies of the top-down equivalent cardiac source approaches, instead suggesting the necessity of the fully coupled approach that is inherent in the physical problem. Macleod placed a perfused dog heart into a tank that was in the shape of a human torso and was filled with electrolyte [67]. The recorded epicardial potential magnitudes changed by 50% when the electrolyte conductivity was doubled, and introducing a pair of balloon insulators near the heart to represent the lungs produced changes in the epicardial potential magnitude of between 8.1% and 20.6%. Throughout these experiments the epicardial activation pattern was stable. In another study, Akiyama noted that placing saline soaked gauze pads on an exposed porcine epicardium significantly reduced the magnitudes of the epicardial potentials [2]. Contact between the epicardium and other conductive tissues within the torso also produced a reduction in the epicardial potential magnitudes. Green measured the epicardial potentials on an isolated, perfused canine heart and also reported no significant changes in the epicardial activation pattern but significant reductions in the magnitude of the epicardial potentials when the heart was moved from an insulating medium to a conducting medium [34].

This experimental evidence can be interpreted from a modeling standpoint by considering that the calculation of an equivalent source in this context is usually performed by the summation of cellular dipoles in an isolated heart. While the patterns of activation will be generally similar between cardiac regions solved in isolation and within a coupled torso, the epicardial potentials will be significantly different and therefore so will the body surface potentials. Given that one of the goals of this modeling is to generate accurate body surface potentials, calculating an equivalent cardiac source from an isolated cardiac model and then using that equivalent source in a torso model is not sufficient for this purpose. It is unlikely that suitable boundary conditions can be placed on the surface of an isolated heart model to properly represent the influence of the ventricular blood masses and passive torso loading on cardiac activation. It is also difficult to quantify the errors associated with placing the extracellular reference potential on the surface of the heart as opposed to the surface of the torso. Only through using a fully coupled approach with boundary conditions in their rightful place on the body surface can more accurate solutions be generated.

Initial model based solutions closely resemble the experimental evidence. Using a fully coupled inhomogeneous model of a slice through the human male torso, an interesting result is achieved when examining the effects of adding realistic lung conductivities as opposed to an average torso conductivity. The lungs contain large amounts of air and therefore are poor electrical conductors. Their conductivities were therefore set to $0.05\,\mathrm{mS\,mm^{-1}}$ (compared with $0.22\,\mathrm{mS\,mm^{-1}}$ for the average torso conductivity). Comparing the results from the two simulations (with and without lungs) revealed average body surface potential magnitude changes of 16.6% and the equivalent change on the epicardium is 17.3% [15]. This epicardial change was within the experimental range that has been found using a torso tank. The traditional two step approach begins with a solution in an isolated heart mesh that knows nothing of the lung conductivities or any other torso components. The cardiac source is then generated, neglecting the large effect the lung conductivities have on the extracellular potential field. As is seen from (14) and (15) which form part of the definition of the bidomain framework, the extracellular potential field is tightly coupled through to the cellular level and therefore changes in the extracellular field have far reaching consequences.

In Fig. 3 another important modeling result is seen. Here the Noble 98 ionic current model [78] has been used within a homogeneous 2D torso slice. The figure displays the body surface potentials over time from one point on the torso that are the result of a two step dipole source solution and

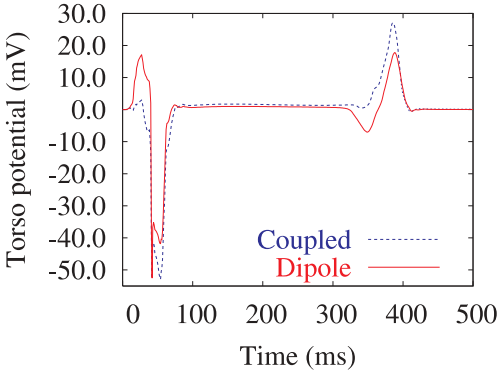

Fig. 3. Body surface potential traces from one node when using an equivalent cardiac source based on multiple moving dipoles (*Dipole*) and a fully coupled solution (*Coupled*). These traces are taken from a 2D torso slice and the dipole trace has been scaled up to match the fully coupled potential magnitudes

a fully coupled solution. The dipole solution is created from 28 dipoles with moving centers and the resulting body surface potentials are scaled up about zero so that the peak absolute potential value on the body surface is the same between the simulations.

While the timing of the events in the two traces is similar, the dipole solution produced much smaller body surface signals and therefore the scaling was necessary. Even after the scaling, Fig. 3 shows that there are quite clearly sections where the two traces have different waveforms, more than enough to be considered clinically significant. While it is acknowledged that the outcomes of simulations in three dimensional may be significantly different, the evidence against a two step approach to solving the forward problem of electrocardiology, both experimental and computational, is mounting. The physical problem is a fully coupled system and it may be necessary to adopt a fully coupled modeling approach to properly quantify the problem.

4.4 Fully coupled approaches

As far as is known, there are at least two groups that have presented results on this fully coupled approach. Both groups are attempting to solve the problem described in (35)–(43), but through different means. These two approaches are now described.

Schematically the complete problem can be divided into four subproblems: The ODEs in H (OH), the parabolic PDE in H (PH), the elliptic PDE in H (EH), and the elliptic PDE in T (ET). These subproblems may be solved fully coupled (which means that for each time step (discrete) solutions are found that simultaneously satisfies all the (discrete) equations. This is accurate but costly. As mentioned above, people have in practice been using operator splitting, i.e. solving each subproblem in sequence. The methods presented below also use this technique to some extent. In particular, the ODE part is always solved separately.

In the first two suggested algorithms (Sects. 4.5.1 and 4.5.2) a tighter coupling is implemented between EP and ET. In the first case by boundary iterations which ensures that EP and ET are satisfied simultaneously. In the second approach the same is achieved by assembling these subproblem into a common linear algebra system (direct assembly). In both cases PH is solve separately.

In the third suggested algorithm (Sect. 4.6) the EP and ET coupling is handled by formulating a scalar PDE whose solution satisfies EP and ET. The coupling with PH is implemented with direct assembly.

4.5 The Auckland approach

Much of the work described in this section is also described in Buist & Pullan [15] *which has been submitted to Annals of Biomedical Engineering*. The different domains present in the forward problem contain important dynamics that occur on different spatial scales. No single solution technique is likely to be the most efficient across all of the scales and therefore descriptions of two new solution methodologies that are based on the coupling of solution techniques that have proven their worth on uncoupled problems are given here. The first new method utilizes an iterative, boundary condition matching approach. Iterations between the extracellular and extramyocardial solutions are undertaken to achieve matching potential fields and current flows across the cardiac surfaces. The second new method treats the problem as a whole where the extracellular domain and all of the extramyocardial regions are assembled directly into a single matrix system. A solution of this matrix system then produces a continuous potential distribution throughout the torso in one step. In some situations it is also useful to combine these two techniques, directly assembling some of the extramyocardial regions and iterating across others. It is important to note that both of these techniques include the torso-heart feedback loop that is omitted from the standard two step approach.

The active cardiac domain is modelled by the bidomain equations which are solved by the *Finite Element Derived Finite Difference Method* [14]. The cardiac geometry is described using a small number of finite elements with high order interpolation functions. A high resolution finite difference grid is then generated in the normalized local element (ξ) space of each finite element. The resulting finite difference mesh may be neither regular or orthogonal in global space, but in the local element space a standard finite difference formulation can be used. Metric tensors transform the spatial derivatives in the bidomain equations into this normalized space. The passive regions that occupy the remainder of the torso volume are governed by a generalized Laplace equation that couples to the extracellular bidomain equation. Tissue regions that are electrically isotropic are modeled using either a standard or derivative boundary element method [114]. The anisotropic regions are modeled using the finite element method and the coupling of the finite and boundary element techniques is described elsewhere [12].

Across the myocardial surfaces, the interface conditions given in (19) and (20) must be satisfied to properly represent the physical situation. Any Dirichlet (potential) interface conditions can be coupled directly though a simple mapping as the cardiac and passive regions both have potential as a dependent variable. While Neumann (current) interface conditions are solved for directly by the boundary element method, the same cannot be said for the finite difference method. Instead an approximation is required to calculate the normal current flow from the cardiac region. Given a conductivity tensor σ and a dependent variable ϕ, a Neumann interface condition can be stated as

$$c = (\sigma \nabla \phi) \cdot n \tag{47}$$

$$= \sigma_i^k \frac{\partial \phi}{\partial \xi^j} \frac{\partial \xi_j}{\partial x^i} n_k \tag{48}$$

where c is the value of the current flow. In traditional formulations a zero current condition is required from the extracellular domain so the value of c is zero. The ξ_j term represents the local element ξ directions within a finite element, and the $\dfrac{\partial \xi_j}{\partial x^i}$ and n_k terms are calculated from the finite element geometry. A fully anisotropic description of the cardiac microstructure is included and σ_i^k is the resultant conductivity tensor after the tensor aligned with the microstructural axes has been rotated into ξ space. The $\dfrac{\partial \phi}{\partial \xi_i}$ term is calculated either by a two point, two-sided or a three point, one-sided differencing scheme de-

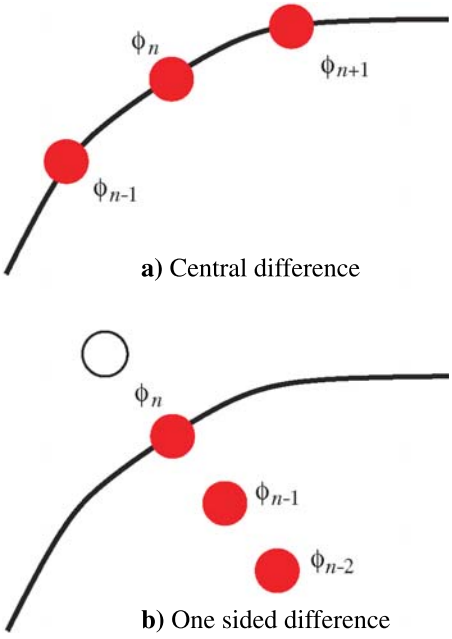

Fig. 4. The $\frac{\partial \phi}{\partial \xi_j}$ term is calculated in each ξ direction using either a central (**a**) or one sided (**b**) differencing scheme based on the availability of points in the direction of interest

pending on the availability of surrounding difference points as is shown in Fig. 4. With these building blocks in place, the details of the two coupling techniques are now given.

4.5.1 Boundary iterations. The first of the coupling techniques is called the method of boundary iterations and seeks to divide the large problem of solving for the extracellular and extramyocardial fields simultaneously into several smaller problems. For the case of the idealized two dimensional torso slice that is illustrated in Fig. 5, the solution domain is divided into three distinct subproblems.

Two problems are set up for the two passive regions, one for region outside the epicardial surface and one for the region

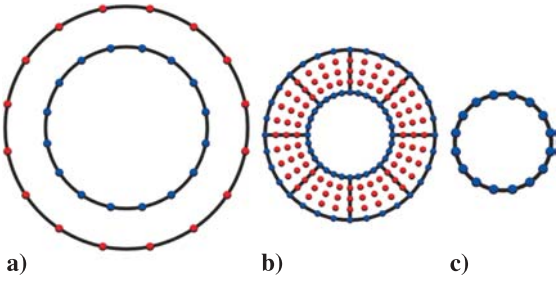

Fig. 5. An idealized view of the three separate problem domains used by the method of boundary iterations. The *left* figure (**a**) shows an annular torso region constructed from two boundary element surfaces where the solution domain lies between the surfaces. The *middle* figure (**b**) shows an annular cardiac region whose geometry is described by finite elements. The finite element derived finite difference technique has then been used to generate the high resolution finite difference solution mesh. The *right* figure (**c**) shows a circular ventricular blood mass region defined by a ring of boundary elements where the solution domain is inside the circle. The complete solution domain is created by placing the ventricular domain inside the annular cardiac domain and then surrounding the cardiac domain with the annular torso domain

enclosed by the endocardial surface. In the annular cardiac region a third problem is set up to solve the bidomain equations. The method of boundary iterations then sets up a fixed point iteration across each of the cardiac surfaces. The aim of the fixed point iterations is to converge until there is no difference between the solutions across the cardiac boundaries. Before any iterations are undertaken a transmembrane equation time step is taken using (15). Then, using the converged epicardial potential solution from the previous time step as an initial guess, the extracellular potential field is calculated from (14). The resulting extracellular field then defines the new boundary conditions on the extramyocardial regions. Both potentials and current flows are passed between the problems creating the fixed point iterations. It has been found that as the solution changes by relatively small amounts with each bidomain time step, only a small number of iterations are required.

In order to minimise the number of computations that are necessary during each iteration, many quantities may be calculated before the start of the iteration process. An efficient mapping is required that relates the boundary element nodes that lie on the cardiac surfaces from the extramyocardial regions to the boundary finite difference points that carry the information from the cardiac region. This is always set up as a one-to-one mapping and is time invariant. An illustration of this is given in Fig. 6.

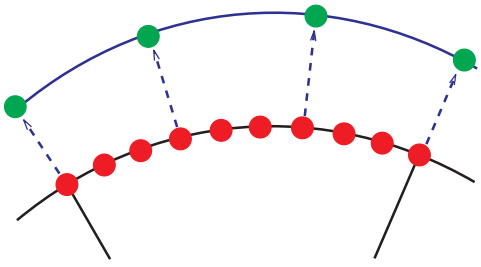

Fig. 6. Multiple difference points may be mapped to each boundary element. Here the curves actually lie on top of each other, representing a finite element boundary and three boundary elements. The *red points* are difference points and the *green points* are boundary element nodes

The mapping in the opposite direction between the boundary finite difference points and the surface boundary elements also does not change over time. As multiple difference points can lie along a single boundary element (as is illustrated in Fig. 6 where four boundary finite difference points map to each boundary element) this mapping can be more complex. The closest adjacent boundary element is found for each boundary finite difference point and a modified Newton iteration is used to calculate the ξ position of the point within the selected element.

With this approach it is necessary for all of the problems to be solved in isolation and therefore some restrictions must be placed on the imposed boundary conditions. The regions outside the epicardium form one problem where the boundary conditions on the torso surface are prescribed by (33) with the addition of some form of reference potential. On the epicardial surface any combination of flux and potential conditions may be imposed on the passive regions surrounding the heart. Each ventricular region must have at least one potential boundary condition to provide a potential reference, but apart from this restriction either a flux or a potential boundary con-

dition can be set at each node on the endocardial surfaces. The boundary conditions set on the epicardial and endocardial surfaces only specify the boundary condition type to be used. The value of the boundary condition is calculated from the finite difference solution and is time and iteration dependent.

The type of boundary conditions set on the surface of the extracellular cardiac domain are derived from the boundary conditions applied to the surrounding extramyocardial surfaces. For example, if the boundary element associated with a given boundary finite difference point has a potential boundary condition set at each local element node then the finite difference point must have a current boundary condition. If each of the local element nodes has a current boundary condition, the finite difference point must have a potential boundary condition. In some situations the local element nodes have different types of boundary conditions applied and in these cases the difference points are assigned boundary conditions based on their ξ location within the coupled boundary element. The convergence of the iteration algorithm relies on this application of complementary boundary conditions to ensure that at a given interface point, both problems are not solving for the same dependent variable. Initially all boundary conditions are set to be consistent with a zero reference potential and no current flow across the outer torso surface.

The solution process is started by incrementing the solution time and solving for the updated cellular variables and transmembrane potential at the new time step. After each time step the iterative process begins anew. If linear elements are used to model the regions surrounding the heart then current and potential values are exchanged across the cardiac boundaries, i.e.,

$$\phi_e \Longleftrightarrow \phi_o \tag{49}$$

$$(\sigma_e \nabla \phi_e) \cdot n_e \Longleftrightarrow -(\sigma_o \nabla \phi_o) \cdot n_o \tag{50}$$

Updating the boundary condition values at the extramyocardial nodes on the cardiac surfaces is a trivial process. If a potential is required at a node it is obtained directly from the extracellular potential of the appropriate coupled finite difference point. If a normal current is required, the finite difference approximation given in (48) is used to calculate the appropriate value. Once all of the passive region boundary values have been updated all passive problems are resolved.

Following the solution of the passive problems, nodal interpolation is used to update the extracellular cardiac boundary conditions as it is quite possible there are more finite difference points than local element nodes within each boundary element. The stored element number and ξ position is used to interpolate the previously calculated nodal fields to find the new boundary values. It is then possible to recalculate a new extracellular potential field that is influenced by the passive torso regions. At the start of each iterative process, the converged extracellular field from the previous time step is used as the initial extracellular solution estimate.

The iterative process continues until the difference between the extracellular and extramyocardial solutions is below specified maximum allowable current and potential tolerances. The solutions fields are compared at each boundary element node on the myocardial surfaces and only when the solution differences are below the tolerances at every node do the iterations cease. As the final extracellular field may be quite different to the initial field, after the iterations have converged the transmembrane potential field is recalculated at the current time step to reflect these differences. Another bidomain time step is then taken and the iterative procedure is restarted. The complete solution algorithm is therefore

foreach time step
  Solve for the transmembrane potential field
    (*Equation* (15))
  while not converged and less than maximum iterations
    Solve for the extracellular potential
      (*Equation* (14))
    Update the cardiac surface nodal boundary conditions(*Equations* (49) *and* (50))
    Solve for a new ventricular solution
      (*Equation* (32))
    Solve for a new torso solution (*Equation* (32))
    Update the extracellular boundary conditions
      (*Equations* (49) *and* (50))
  end while
  Solve for the transmembrane potential
    (*Equation* (15))
end foreach

It has been found that it is necessary to add relaxation parameters to the iteration algorithm to prevent oscillations. These effectively reduce the step size taken each time boundary conditions are transferred, moving only part of the way towards the solution suggested by the other region. The first parameter, α_1, applies to obtaining cardiac boundary conditions from the boundary elements and the second parameter, α_2, applies to obtaining nodal boundary conditions from the finite difference solution. In both cases (51) is used with the α_i $(= \alpha_1, \alpha_2)$ parameter always multiplying the finite difference contribution.

$$\phi = (\alpha_i)\,\phi_e + (1 - \alpha_i)\,\phi_o \tag{51}$$

These parameters introduce a trade off between convergence stability and speed. In the extreme case of $\alpha_1 = 1.0$ or $\alpha_2 = 0.0$, no progress can be made towards the converged solution. It is envisaged that the lowest value of α_1 and the highest value of α_2 that maintains convergence will allow the largest steps to be taken and therefore the fastest convergence.

4.5.2 Direct assembly. While the boundary iteration approach divides the forward problem into smaller pieces, the direct assembly approach seeks to couple the different problem regions by assembling all of the equations from the extracellular and extramyocardial domains into a single matrix system. The application of the interface conditions from (19) and (20) are an integral part of the resulting matrix structure. Given a transmembrane potential distribution, this matrix system directly returns solutions that are continuous across the cardiac boundaries. The methods by which the extracellular finite difference equations and the extramyocardial boundary element equations are coupled are presented here.

The direct assembly method eliminates the need to perform multiple solutions at each time step and also avoids the additional book keeping that is necessary with the iterative process. The main disadvantage with this approach is that the solution matrix is significantly larger than the matrices from the iterative approach and they contain large dense regions due to the boundary elements and the imposition of the coupling conditions. With the current implementation it has been assumed that there is a one to one mapping between the boundary finite difference points and the surrounding boundary element nodes to which they are coupled. Here two cases are used to illustrate the formulation of the direct assembly method. In the first case we consider an active cardiac region that completely encloses a passive ventricular region, and in the second case an additional passive region is added that surrounds the cardiac region.

An idealized occurrence of the first scenario is illustrated in Fig. 7 where a single circular boundary element ventricular region is completely enclosed by an annular cardiac region. The finite difference points in the cardiac region are placed into one of several classes based on their location with respect to the cardiac surfaces. Boundary finite difference points that are not coupled to boundary element nodes are given the subscript h and the corresponding matrix coefficients are denoted by K_h. Boundary finite difference points connected to boundary element nodes are given the subscript b with matrix coefficients K_b. Internal finite difference points that are used in the finite difference approximations of the normal boundary currents are given the subscript j and matrix coefficients K_j. Any remaining finite difference points are internal and are not directly involved in the boundary element coupling. These points are given the subscript I with coefficients K_I.

The governing equation for the extracellular potential field, ϕ_e, in the cardiac region is given by (14) and results in a matrix system of the form

$$K\phi = f \tag{52}$$

where K is the matrix of finite difference coefficients, ϕ is the vector of extracellular potentials and f is calculated from the transmembrane potential field and boundary conditions that have been applied. The K matrix can then be expressed in terms of the finite difference groupings as

$$\begin{bmatrix} K_{hh} & K_{hI} & K_{hj} & K_{hb} \\ K_{Ih} & K_{II} & K_{Ij} & K_{Ib} \\ K_{jh} & K_{jI} & K_{jj} & K_{jb} \\ K_{bh} & K_{bI} & K_{bj} & K_{bb} \end{bmatrix} \begin{bmatrix} \phi_h \\ \phi_I \\ \phi_j \\ \phi_b \end{bmatrix} = \begin{bmatrix} f_h \\ f_I \\ f_j \\ f_b \end{bmatrix} .$$

If the internal boundary element region is considered in isolation, a system of equations would normally be created to solve the generalized Laplace equation given by (32), where the coefficients can be assembled into a matrix system of the form

$$G\phi = Hq\,. \tag{53}$$

Here ϕ represents the potential field and G is the matrix of the potential field coefficients, q represents the normal boundary flux at each node and H is the matrix of flux coefficients. Boundary conditions would usually be applied to (53) to form a square $b \times b$ system of equations to be solved. In the coupled problem b is both the number of boundary element nodes and the number of coupled finite difference points. Each element of the q vector of fluxes can be described in terms of a finite difference approximation from (48). The coefficients from these approximations are assembled into a matrix, D, where each row in D is generated from a boundary finite difference point coupled to a boundary element node, and the values in each row are the finite difference flux coefficients. The D matrix therefore has b rows and $(b+j)$ columns. The continuity of current interface condition can now be written as

$$q = -D\phi\,. \tag{54}$$

Here it has been assumed that both the cardiac and the boundary element regions are defined with outward normal vectors so the negative sign is required to reflect the direction of the current flow. Combining (53) and (54) gives

$$\begin{aligned} Hq &= -HD\phi \\ &= \begin{bmatrix} H_{bb} \end{bmatrix} \begin{bmatrix} -D_{bb} & -D_{bj} \end{bmatrix} \begin{bmatrix} \phi_b \\ \phi_j \end{bmatrix} \\ &= \begin{bmatrix} -H_{bb}D_{bb} & -H_{bb}D_{bj} \end{bmatrix} \begin{bmatrix} \phi_b \\ \phi_j \end{bmatrix} \end{aligned} \tag{55}$$

and substitution back into (53) gives

$$\begin{bmatrix} G_{bb} & 0 \end{bmatrix} \begin{bmatrix} \phi_b \\ \phi_j \end{bmatrix} = \begin{bmatrix} -H_{bb}D_{bb} & -H_{bb}D_{bj} \end{bmatrix} \begin{bmatrix} \phi_b \\ \phi_j \end{bmatrix} . \tag{56}$$

Rearranging (56) gives the expressions for the coupled boundary points in terms of potentials over the finite difference mesh, i.e.,

$$\begin{bmatrix} G_{bb} + H_{bb}D_{bb} & H_{bb}D_{bj} \end{bmatrix} \begin{bmatrix} \phi_b \\ \phi_j \end{bmatrix} = 0\,. \tag{57}$$

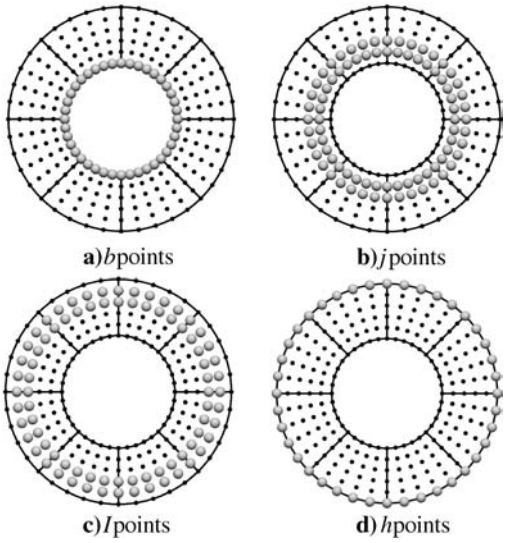

Fig. 7. A simple annular finite element mesh enclosing a circular boundary element mesh. The finite difference points of interest are drawn enlarged. The *first* figure (**a**) shows type b finite difference points that are coupled to boundary elements. The *second* figure (**b**) shows type j finite difference points that are used to calculate normal boundary fluxes. The *third* figure (**c**) shows type I finite difference points that are internal and not involved on any coupling, and the *fourth* figure (**d**) shows type h finite difference points that are external but are uncoupled

This expression is then assembled into the finite difference coefficient matrix from (52) to obtain the final system.

$$\begin{bmatrix} K_{hh} & K_{hI} & K_{hj} & K_{hb} \\ K_{Ih} & K_{II} & K_{Ij} & K_{Ib} \\ K_{jh} & K_{jI} & K_{jj} & K_{jb} \\ 0 & 0 & H_{bb}D_{bj} & G_{bb}+H_{bb}D_{bb} \end{bmatrix} \begin{bmatrix} \phi_h \\ \phi_I \\ \phi_j \\ \phi_b \end{bmatrix} = \begin{bmatrix} f_h \\ f_I \\ f_j \\ 0 \end{bmatrix} \tag{58}$$

Equation (58) is actually a simplified view of the matrix structure. Because of independent node and finite difference point numbering systems, the G and H matrices have their rows and columns pivoted to prepare them for assembly into the K matrix, which is assembled in an ascending finite difference point order. The global finite difference point numbers within each classification are also not contiguous. Throughout the assembly process only dense matrices are not stored in sparse structures to allow large problems to be solved. The right hand side vector components, f_I and f_j are found from (14) and for f_h, any potential or current boundary conditions may be applied.

The addition of an external region that surrounds both the cardiac and the ventricular regions results in a three component problem that is illustrated in Fig. 5. Instead of iterating across the two cardiac surfaces, all three regions are directly assembled into a single solution matrix. In situations such as this where all of the cardiac boundaries are coupled there are no h finite difference points as they are all coupled to boundary element nodes. The torso surface nodes are not directly coupled to a finite difference point and are assigned global numbers that are consistent with the finite difference point numbering system. This allows them to be assembled into the final finite difference based solution matrix. The torso surface points are given the subscript t with matrix coefficients G_t and H_t.

If the boundary element coefficient matrices from the ventricular region are denoted by $G1$ and $H1$, and the matrices from the torso regions are denoted by $G2$ and $H2$ then these can be assembled into global G and H matrices of the form

$$\begin{bmatrix} G1_{bb} & 0 & 0 \\ 0 & G2_{bb} & G2_{bt} \\ 0 & G2_{tb} & G2_{tt} \end{bmatrix} \begin{bmatrix} \phi_{1b} \\ \phi_{2b} \\ \phi_{2t} \end{bmatrix} = \begin{bmatrix} H1_{bb} & 0 & 0 \\ 0 & H2_{bb} & H2_{bt} \\ 0 & H2_{tb} & H2_{tt} \end{bmatrix} \begin{bmatrix} q_{1b} \\ q_{2b} \\ q_{2t} \end{bmatrix} \tag{59}$$

The torso element matrix system can now be thought of in terms of coupled (b) and uncoupled (t) nodes.

$$\begin{bmatrix} G_{bb} & G_{bt} \\ G_{tb} & G_{tt} \end{bmatrix} \begin{bmatrix} \phi_b \\ \phi_t \end{bmatrix} = \begin{bmatrix} H_{bb} & H_{bt} \\ H_{tb} & H_{tt} \end{bmatrix} \begin{bmatrix} q_b \\ q_t \end{bmatrix} \tag{60}$$

The outer surface of the torso domain is assumed to have an insulating air boundary and therefore the q_t values are zero. The coupling conditions are then formulated to find an expression equivalent to (55).

$$\begin{aligned} Hq &= -\begin{bmatrix} H_{bb} & H_{bt} \\ H_{tb} & H_{tt} \end{bmatrix} \begin{bmatrix} D_{bb} & D_{bj} & 0 \\ 0 & 0 & 0 \end{bmatrix} \begin{bmatrix} \phi_b \\ \phi_j \\ \phi_t \end{bmatrix} \\ &= -\begin{bmatrix} H_{bb}D_{bb} & H_{bb}D_{bj} & 0 \\ H_{tb}D_{bb} & H_{tb}D_{bj} & 0 \end{bmatrix} \begin{bmatrix} \phi_b \\ \phi_j \\ \phi_t \end{bmatrix} \end{aligned} \tag{61}$$

This system is then combined with the G matrix to obtain an equation in the same form as (57).

$$(G+HD)\,\phi = 0$$

$$\begin{bmatrix} G_{bb}+H_{bb}D_{bb} & H_{bb}D_{bj} & G_{bt} \\ G_{tb}+H_{tb}D_{bb} & H_{tb}D_{bj} & G_{tt} \end{bmatrix} \begin{bmatrix} \phi_b \\ \phi_j \\ \phi_t \end{bmatrix} = 0 \tag{62}$$

This result is then assembled into the global matrix system, K to obtain the final system shown in (63).

$$\begin{bmatrix} K_{II} & K_{I1j} & K_{I2j} & K_{I1b} & K_{I2b} & 0 \\ K_{1jI} & K_{1j1j} & K_{1j2j} & K_{1j1b} & K_{1j2b} & 0 \\ K_{2jI} & K_{2j1j} & K_{2j2j} & K_{2j1b} & K_{2j2b} & 0 \\ 0 & H_{1bb}D_{1bj} & 0 & G_{1bb}+H_{1bb}D_{1bb} & 0 & 0 \\ 0 & 0 & H_{2bb}D_{2bj} & 0 & G_{2bb}+H_{2bb}D_{2bb} & G_{2bt} \\ 0 & 0 & H_{2tb}D_{2bj} & 0 & G_{2tb}+H_{2tb}D_{2bb} & G_{2tt} \end{bmatrix}$$

$$\times \begin{bmatrix} \phi_I \\ \phi_{1j} \\ \phi_{2j} \\ \phi_{1b} \\ \phi_{2b} \\ \phi_t \end{bmatrix} = \begin{bmatrix} f_I \\ f_{1j} \\ f_{2j} \\ 0 \\ 0 \\ 0 \end{bmatrix} \tag{63}$$

The physical problem requires some sort of reference potential on the surface of the torso and here a single reference node is set to have a zero potential. The matrix row and column that correspond to this reference are eliminated from the final matrix system during the assembly process and the consistency criteria of Salu is again used to generate solutions consistent with the system of equations [95].

4.6 The Oslo approach

It is possible to solve the PDEs of the bidomain model simultaneously with a fully implicit approach. In theory it is possible to also include the cell model ODEs in such a simultaneous discretization, for a fully implicit solution of the complete problem. However, most ionic current models are non-linear and highly complex, and it is convenient to separate these equations from the PDEs with an operator splitting technique. Such a semi-implicit technique may be described as follows.

1. Assume that the solution of V_m and s at time t_n is known.
2. Integrate the cell model ODEs with a suitable solver for stiff ODE systems, to obtain the state vector s at time step t_{n+1}.
3. Solve the PDEs fully coupled to determine the unknown fields V_m^{n+1}, ϕ_e^{n+1} and ϕ_o^{n+1}.

A possible choice of solver for the stiff ODE systems is described in [110]. To discretize the PDEs we combine an implicit Euler time discretization with a finite element discretization in space [111]. Recall that the PDEs in (35)–(43) are linear except for the ionic current term $I_{\text{ion}}(V_m, s)$. To avoid solving non-linear equations for each time step we evaluate this term explicitly, i.e. $I_{\text{ion}}(V_m^n, s^{n+1})$. Because s^{n+1} is already known we then have no problems with non-linearity.

With this approach we get a time discrete PDE system given by

$$\nabla\cdot\left(\sigma_i'\nabla V_m^{n+1}\right)+\nabla\cdot\left(\sigma_i'\nabla\phi_e^{n+1}\right) = A_m\frac{V_m^{n+1}-V_m^n}{\Delta t}+A_m' I_{\text{ion}}\left(V_m^n, s^{n+1}\right) \quad x\in H\,, \tag{64}$$

$$\nabla\cdot\left(\sigma_i'\nabla V_m^{n+1}\right)+\nabla\cdot\left(\left(\sigma_i'+\sigma_e'\right)\nabla\phi_e^{n+1}\right)=0 \quad x\in H\,, \tag{65}$$

$$\nabla\cdot\left(\sigma_o'\nabla\phi_o^{n+1}\right)=0 \quad x\in T\,, \tag{66}$$

$$n_H\cdot\left(\sigma_i'\nabla V_m^{n+1}+\sigma_i'\nabla\phi_e^{n+1}\right)=0 \quad x\in\partial H\,, \tag{67}$$

$$\phi_e^{n+1}=\phi_o^{n+1} \quad x\in\partial H\,, \tag{68}$$

$$n_H\cdot\left(\sigma_e'\nabla\phi_e^{n+1}\right)+n_T\cdot\left(\sigma_o'\nabla\phi_o^{n+1}\right)=0 \quad x\in\partial H\,, \tag{69}$$

$$n_T\cdot\left(\sigma_o'\nabla\phi_o^{n+1}\right)=0 \quad x\in\partial T\,. \tag{70}$$

The primes on the A_m and the conductivity tensors are introduced because we have scaled the equations with the membrane capacitance C_m. The new quantities are defined by

$$\sigma_i'=\frac{1}{C_m}\sigma_i\,, \qquad \sigma_e'=\frac{1}{C_m}\sigma_e\,,$$
$$\sigma_o'=\frac{1}{C_m}\sigma_o\,, \qquad A_m'=\frac{1}{C_m}A_m\,.$$

For the remainder of this section we will skip the primes on the symbols, as we will always refer to the scaled quantities.

We may use a standard Galerkin finite element method to obtain a spatial discretization of the time discrete system. To obtain a weak formulation of the equations we introduce appropriate function spaces $V(H)$ and $V(T)$ such that $V_m, \phi_e\in V(H)$ and $\phi_o\in V(T)$. To simplify the notation we also introduce the inner products

$$(v,\varphi)=A_m\int_H v\varphi dx\,, \tag{71}$$

$$a_i(v,\varphi)=\int_H \sigma_i\nabla v\cdot\nabla\varphi dx\,, \tag{72}$$

$$a_{i+e}(v,\varphi)=\int_H (\sigma_i+\sigma_e)\nabla v\cdot\nabla\varphi dx\,, \tag{73}$$

$$a_T(v,\varphi)=\int_T \sigma_o\nabla v\cdot\nabla\varphi dx\,. \tag{74}$$

A weak formulation of (64)–(66) may then be written

$$-a_i\left(V_m^{n+1},\varphi\right)-a_i\left(\phi_e^{n+1},\varphi\right) +\int_{\partial H}\varphi\left[\left(\sigma_i\nabla V_m^{n+1}\right)\cdot n_H+\left(\sigma_i\nabla\phi_e^{n+1}\right)\cdot n_H\right]dS = \frac{1}{\Delta t}\left(V_m^{n+1}-V_m^n,\varphi\right)+\left(\varphi, I_{\text{ion}}\left(V_m^n,s^{n+1}\right)\right) \quad \forall\varphi\in V(H)\,, \tag{75}$$

$$-a_i\left(V_m^{n+1},\varphi\right)-a_{i+e}\left(\phi_e^{n+1},\varphi\right) +\int_{\partial H}\varphi\left[\left(\sigma_i\nabla V_m^{n+1}\right)\cdot n_H+\left(\sigma_i\nabla\phi_e^{n+1}\right)\cdot n_H\right]dS +\int_{\partial H}\varphi\left[\left(\sigma_e\nabla\phi_e^{n+1}\right)\cdot n_H\right]dS=0 \quad \forall\varphi\in V(H)\,, \tag{76}$$

$$-a_T\left(\phi_o^{n+1},\varphi\right)+\int_{\partial H}\varphi\left[\left(\sigma_o\nabla\phi_o^{n+1}\right)\cdot n_T\right]dS +\int_{\partial T}\varphi\left[\left(\sigma_o\nabla\phi_o^{n+1}\right)\cdot n_T\right]dS=0 \quad \forall\varphi\in V(T)\,. \tag{77}$$

The weakly formulated equations may be simplified by applying the conditions specified on the surface of the heart and the torso. The boundary integral in (75) and the first of the two boundary terms in (76) vanish because of the boundary condition (67). Furthermore, the boundary integral over ∂T vanishes because of (70). The system is reduced to

$$-a_i\left(V_m^{n+1},\varphi\right)-a_i\left(\phi_e^{n+1},\varphi\right) =\frac{1}{\Delta t}\left(V_m^{n+1}-V_m^n,\varphi\right)+\left(\varphi, I_{\text{ion}}\left(V_m^n,s^{n+1}\right)\right) \quad \forall\varphi\in V(H)\,, \tag{78}$$

$$-a_i\left(V_m^{n+1},\varphi\right)-a_{i+e}\left(\phi_e^{n+1},\varphi\right) +\int_{\partial H}\varphi\left[\left(\sigma_e\nabla\phi_e^{n+1}\right)\cdot n_H\right]dS=0 \quad \forall\varphi\in V(H)\,, \tag{79}$$

$$-a_T\left(\phi_o^{n+1},\varphi\right)+\int_{\partial H}\varphi\left[\left(\sigma_o\nabla\phi_o^{n+1}\right)\cdot n_T\right]dS=0 \quad \forall\varphi\in V(T)\,. \tag{80}$$

Equation (68) states that on the heart surface the extracellular potential is equal to the potential in the surrounding torso. We may introduce a new field ϕ, defined over $H\cup T$, given by

$$\phi=\begin{cases}\phi_e & \text{in } H\\ \phi_o & \text{in } T\end{cases}\,.$$

If we add (79) and (80), the weakly formulated system is reduced to two equations. The remaining boundary integral terms cancel due to the continuity condition (69). We get

$$\left(V_m^{n+1},\varphi\right)+\Delta t a_i\left(V_m^{n+1},\varphi\right)+\Delta t a_i\left(\phi^{n+1},\varphi\right) =\left(V_m^n,\varphi\right)-\Delta t\left(\varphi, I_{\text{ion}}\left(V_m^n,s^{n+1}\right)\right) \quad \forall\varphi\in V(H)\,, \tag{81}$$

$$\Delta t a_i\left(V_m^{n+1},\varphi\right)+\Delta t a_{i+e}\left(\phi^{n+1},\varphi\right) +\Delta t a_T\left(\phi^{n+1},\varphi\right)=0 \quad \forall\varphi\in V(H\cup T)\,, \tag{82}$$

where both equations have been multiplied with Δt.

As stated in (73) and (74), $a_{i+e}(\cdot,\cdot)$ is defined as an integral over H while $a_T(\cdot,\cdot)$ is an integral over T. Accordingly, the terms $a_{i+e}(\phi^{n+1},\varphi)$ and $a_T(\phi^{n+1},\varphi)$ are non-zero only for test functions φ with support in H and T, respectively. Both terms will be non-zero if φ has support in both H and T.

To discretize the weakly formulated equations we introduce two grids, one over H and one over $H\cup T$. We define basis functions ψ_i, $i=1,\ldots,m$ and η_i, $i=1,\ldots,n$, which

span discrete subspaces of $V(H)$ and $V(H \cup T)$ respectively. The unknown fields V_m^{n+1} and ϕ^{n+1} may be approximated by

$$V_m^{n+1} = \sum_{i=1}^{p} \psi_i v_i \tag{83}$$

$$\phi^{n+1} = \sum_{i=1}^{q} \eta_i u_i \,. \tag{84}$$

Inserting these approximations into the weak formulation given above, we obtain the block structured linear system

$$\mathcal{A} \begin{bmatrix} v \\ u \end{bmatrix} = \begin{bmatrix} A & B \\ B^T & C \end{bmatrix} \begin{bmatrix} v \\ u \end{bmatrix} = \begin{bmatrix} \alpha \\ 0 \end{bmatrix} . \tag{85}$$

The blocks are given by

$$A_{ij} = \left(\psi_i, \psi_j\right) + \Delta t a_i \left(\psi_i, \psi_j\right) , \tag{86}$$

$$B_{ij} = \Delta t a_i \left(\psi_i, \eta_j\right) , \tag{87}$$

$$C_{ij} = \Delta t a_{i+e} \left(\eta_i, \eta_j\right) + \Delta t a_T \left(\eta_i, \eta_j\right) , \tag{88}$$

and the right hand side vector

$$\alpha_i = \left(v^n, \psi_i\right) - \Delta t \left(\psi, I_{\text{ion}} \left(v^n, s^{n+1}\right)\right) .$$

We see that A has dimension $m \times m$, B $m \times n$ and C is an $n \times n$ matrix. Since we normally have $m \neq n$, B and B^T are rectangular matrices.

The structure of the linear system presented here is fairly complex, and a common method for solving such systems is to apply some sort of operator splitting technique. By simple techniques like e.g. block Jacobi iterations, defined for the present system by

$$v^{k+1} = A^{-1} \left(\alpha - B u^k\right) , \tag{89}$$

$$u^{k+1} = C^{-1} \left(-B^T v^k\right) , \tag{90}$$

it is possible to reduce the complex coupled system to two simpler systems. It is then often possible to construct efficient solution algorithms for solving these sub-systems, i.e. for computing the inverses A^{-1} and C^{-1}. However, even if the sub-systems may be solved efficiently, the convergence of the operator splitting algorithm itself may in many cases be slow. To avoid such problems, we have proposed to use the block Jacobi iteration as a preconditioner for a Krylov-subspace iterative method, rather than as a solver in itself. The inverses A^{-1} and C^{-1} are then approximated with a fixed number of multigrid cycles. In matrix form, the suggested preconditioner may be written

$$\mathcal{B} = \begin{bmatrix} \widehat{\left(A^{-1}\right)} & 0 \\ 0 & \widehat{\left(C^{-1}\right)} \end{bmatrix} ,$$

where $\widehat{(\cdot)}$ denotes a multigrid approximation to the respective inverse. Because of the symmetry of the operators $a_i(\cdot,\cdot)$, $a_{i+e}(\cdot,\cdot)$ and $a_T(\cdot,\cdot)$, the linear system (85) is obviously symmetric. This also applies to the preconditioned system

$$\mathcal{B}\mathcal{A} \begin{bmatrix} v \\ u \end{bmatrix} = \mathcal{B} \begin{bmatrix} \alpha \\ 0 \end{bmatrix} ,$$

to which we apply the iterative solver. Preliminary analysis indicates that the system is also positive definite, and we have thus chosen the Conjugate Gradient (CG) method to solve the linear system. Although the positivity of the system remains to be formally verified, experimental results confirm that the CG algorithm performs well.

The fully coupled solution technique presented here has been tested for a number of problems differing in complexity and physiological relevance. The obtained results demonstrate that the scaling properties of the algorithm are very close to being optimal, in the sense that the workload is linear with respect to the number of unknowns. Results from a 3D simulation on a realistic geometry are shown in Fig. 8. For this simulation the geometry and fiber directions of the ventricles were taken from [76], and the geometry of the torso was constructed from the Visible Human dataset [122]. A relatively coarse grid with 83 025 unknowns in the heart and 473 738 nodes in the torso has been used. The time instant shown is after 20 ms and after time step number 160.

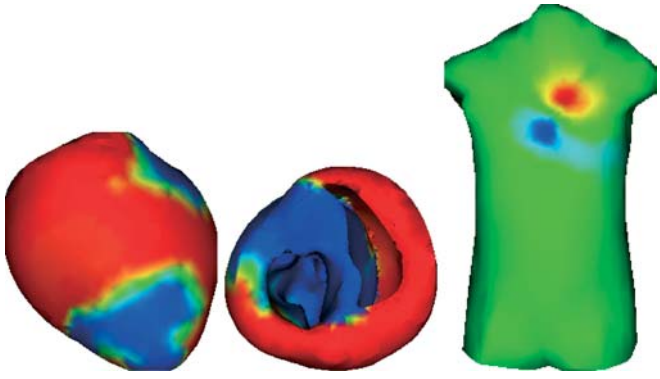

Fig. 8. The transmembrane potential and the body surface potential after 20 ms. The heart is view from the front and from above. Both on the heart and on the torso *red* and *blue* indicates negative and positive potentials, respectively

5 Presentation and visualization of results

Solutions to the forward problem generate huge amounts of data, often on the order of several gigabytes. Time dependent data is generated from each individual cell through to all of the solution points within the torso. Binary file formats allow the generated information to be stored efficiently but perhaps the best solution to this data problem is to decide what information will be required before any simulations are run. Often not all of the data is necessary and it is possible to only store the information of interest, for example only storing body surface potential traces while omitting much cellular information. The way in which the resulting data is displayed depends on what information is most useful to the viewer and has some element of personal preference. Here several of the visualization techniques commonly used in this field are illustrated to give an idea of what sorts of displays are possible.

The first illustration is shown in Fig. 9 shows two views of the torso model developed at The University of Auckland which is constructed from high order finite and boundary elements. The left figure (Fig. 9a) shows the full inhomogeneous torso mesh including a cardiac region, two lung regions, a torso cavity, an anisotropic skeletal muscle later and

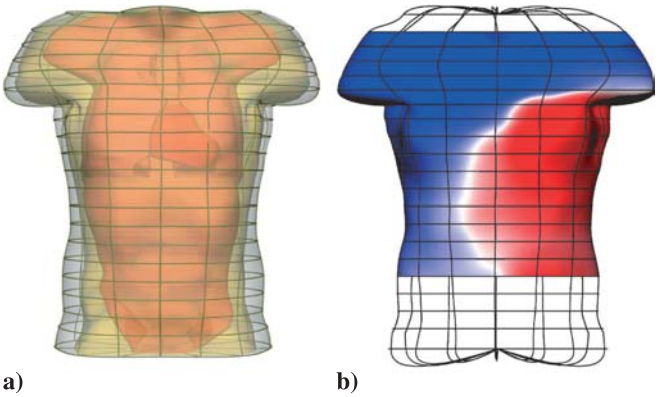

a) **b)**

Fig. 9. The *left* figure (**a**) shows the full inhomogeneous Auckland torso model. The *right* figure (**b**) shows a body surface map that was recorded from a normal volunteer

a subcutaneous fat layer. One of the applications of this model is the interpretation of experimentally recorded body surface maps. The right figure (Fig. 9b) shows one way of representing a body surface potential map that has been recorded off a normal volunteer, using a 256 electrode jacket and fitting the recorded potentials to the torso surface. Here white represents a zero potential value, blue represents negative potentials and red represents positive potentials.

Figure 10 shows two pictures from the same torso that is used in Fig. 9a. Here computed body surface potential fields are drawn at one time instant, where again blue potentials are negative and red potentials are positive. Over the body surface potential field, contours of constant potential have been drawn using black lines. Figure 10a shows the contours on the front of the torso and Fig. 10b shows the contours on the back of the torso where both pictures are drawn using data from the same time step. In addition to drawing these potential fields and contours on the torso surface, it is also possible to draw them on the epicardial surface or any of the other region surfaces within the torso.

Often it is useful to use transparency to look at what is happening within the torso cavity. An illustration of this given in Fig. 11a. Here colored isosurfaces are drawn through two potential values within the torso geometry. This can be thought of as a 3D representation of what the contour lines show on the surface of the torso and gives a way of visualizing how potential lines on the epicardium are mapped out to the body surface. In Fig. 11b the torso surface has been made transparent again in order to see lines of constant current drawn within the torso. Here the current lines link the areas of the heart that have positive and negative potentials. These current lines are started from either fixed or random seed points and give an indication of the current loops within the torso that result from cardiac electrical activity.

At the level of the heart it is possible to draw either the transmembrane potential field (as is shown in Fig. 12a) or extracellular potential field on the surface of the myocardium. Here the Noble 98 cellular model is used with a 40 finite element description of the myocardium over which the finite element derived finite difference method has been used to create a high resolution mesh. The blue tissue is at the resting potential and the red tissue is at the peak potential. Any of the cellular parameters can also be plotted over the cardiac mesh so features such as the calcium wave can be visualized. One other option is to calculate the activation times of each of the cardiac solution points and it is then possible to draw the activation times as a field over the cardiac geometry. This situation is illustrated in a 2D cross section through the heart in Fig. 12b where blue regions are early activation times and yellow regions are late activation times. The contours are drawn at uniform time intervals.

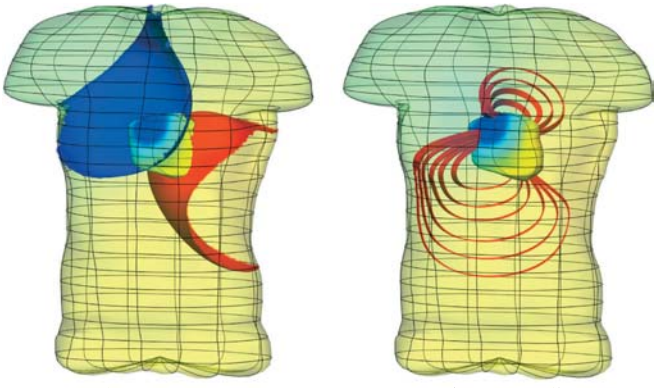

a) ϕ_0 isosurfaces **b)** Current lines

Fig. 11. The *left* figure (**a**) shows calculated potential isosurfaces within a homogeneous torso that are the result of a cardiac source. The *right* figure (**b**) shows current lines within the torso that start and end in the heart as a result of the zero flux torso surface boundary conditions

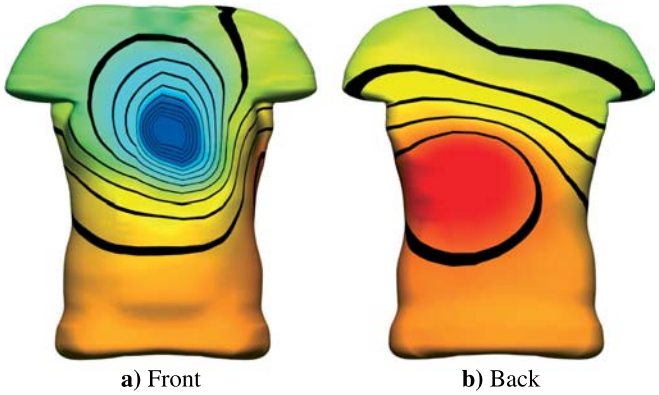

a) Front **b)** Back

Fig. 10. These figures show the calculated potential field on the front and back surfaces of the torso where contours have been drawn at constant potential intervals

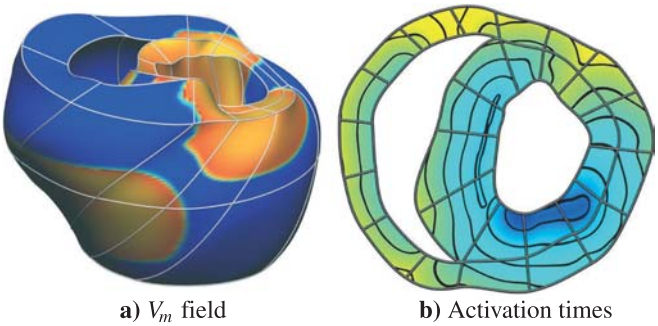

a) V_m field **b)** Activation times

Fig. 12. The *left* figure (**a**) shows the transmembrane potential field on the surface of the Auckland ventricular model. Here the Noble 98 cellular model is used. The *right* figure (**b**) shows a slice through the ventricular model onto which a field showing calculated activation times has been drawn

Figure 13 demonstrates the use of an isosurface to show the position of the wavefront as it moves through a block of myocardium. In this case the block is the inter-ventricular septum from the Auckland heart model and into this domain an idealized Purkinje fiber tree is grown. The terminal branches of the tree are coupled to the myocardium so that stimulation to the proximal end of the tree will start an activation wave that traverses the tree and then activates the myocardial tissue. The semi-transparent surfaces on the tissue block in this situation have been colored by the transmembrane potential field where blue tissue is at rest and red tissue is at the plateau potential. The three pictures shown in Fig. 13 show the position of the activation wave 25, 30 and 40 ms after a stimulation has been applied to the proximal end of the Purkinje tree.

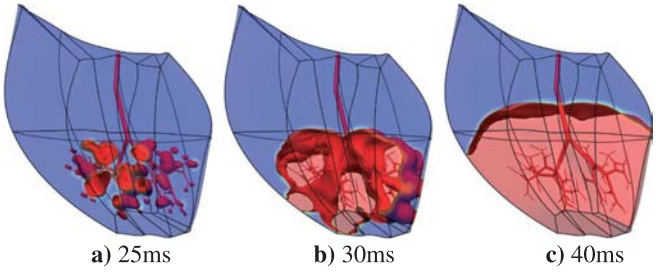

Fig. 13. These figures show three time instants in the activation of the ventricular septum from the Auckland heart model. Here an idealised Purkinje tree is coupled to the myocardium at the distal ends of the tree

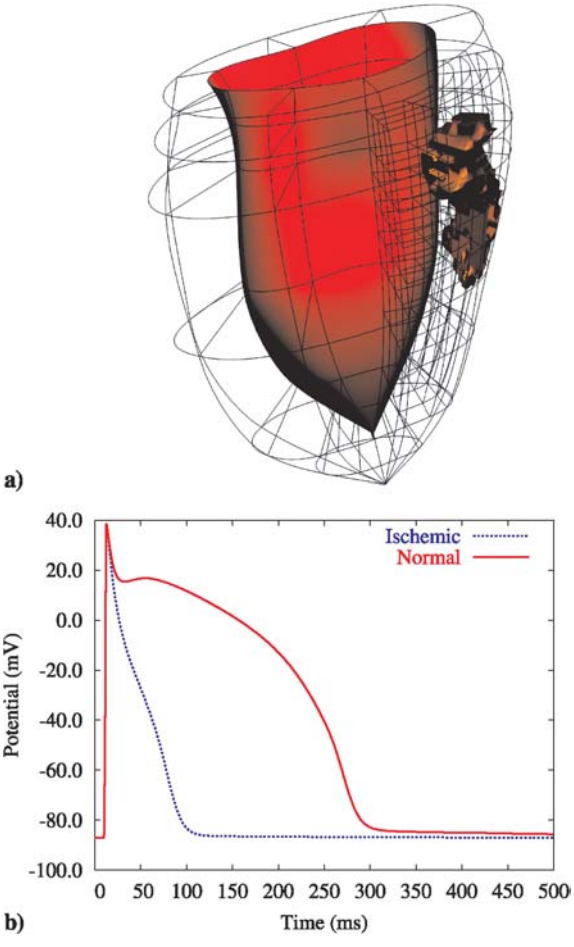

Fig. 14. The *first* figure (**a**) shows the local refinement of the solution mesh around an infarcted region in the left ventricular wall. The *second* figure (**b**) shows the cellular action potential from the Beeler–Reuter [9] model in normal and ischemic tissue. The picture in figure **a** is courtesy of Carey Stevens, The University of Auckland

One current application area is the study of myocardial ischemia and infarction. Figure 14a shows a porcine left ventricle where an infarcted region is present within the myocardial wall. The location and geometry of the infarct is determined from experimentally obtained slices. An adaptive meshing technique is used to increase the finite element resolution around the area of interest so the infarct geometry is well defined. It is then possible to adjust the cellular parameters to reflect material property changes that occur in the infarct, and in the ischemic border zone around the infarct. Fig. 14b shows the cellular model developed by Beeler & Reuter [9] in normal and ischemic tissue. This change in the action potential is achieved by reducing the conductance of the slow inward current.

6 Discussion

We have described the forward problem of cardiac electrophysiology and reviewed the current state of this research area. We have presented above how the inherently coupled nature of the current flow through the heart and torso may be modeled and solved. The size of this problem currently prevents a full solution of this model in 3D even using the middle-out modeling approach adopted here. We have also focussed solely on the electrical activity. However, cardiac activity is a highly complicated and coupled problem, and factors such as mechanics, energetics, fluid flow all affect the electrical and geometric nature of the problem. The mechanics changes the geometry of the heart and thus also the conductivity tensors and the propagation. Furthermore, the blood flow is coupled to the mechanical behavior of the heart.

One often hears such limitations being used as reasons for dismissing a models utility outright. The forward problem presented here is a step towards the virtual heart. It must be the way forward – there is no other feasible way of dealing with the emerging volumes of data in any sensible sort of manner.

With the steady advance in hardware and software we believe that the field of electrocardiology will find computations increasingly useful and necessary. First as a research tool, but ultimately also in clinical use.

References

1. Adams, D.R.: Propagation of Depolarization and Repolarization Processes in the Myocardium – An Anisotropic Model. IEEE Trans. Biomed. Eng. 38(2), 133–141 (1991)
2. Akiyama, T., Richeson, J.F., Ingram, J.T., Oravec, J.: Effects of varying the electrical conductivity of the medium between the heart and the body surface on the epicardial and praecordial electrocardiogram in the pig. Cardiovasc. Res. 12, 697–702 (1978)
3. Antzelevitch, C., Sicouri, S., Litovsky, S., Lukas, A., Krishnan, S., Diego, J., Gintant, G., Liu, D.: Hetrogeneity Within the Ventricular Wall. Electrophysiology and Pharmacology of Epicardial, Endocardialm and M Cells. Circ. Res. 69(6), 1427–1449 (1991)
4. Barr, R.C., Plonsey, R.: Propagation of excitation in idealized anisotropic two-dimnesional tissue. Biophys. J. 45, 1191–1202 (1984)

5. Barr, R.C., Pilkington, T.C., Boineau, J.P., Spach, M.S: Determining Surface Potentials from Current Dipoles, with application to Electrocardiography. IEEE Trans. Biomed. Eng. 13(2), 88–92 (1966)
6. Barr, R.C., Ramsey, M., Spach, M.S: Relating Epicardial to Body Surface Potential Distributions by Means of Transfer Coefficients Based on Geometry Measurements. IEEE Trans. Biomed. Eng. 24(1), 88–92 (1977)
7. Basser, P.J., Mattiello, J., Bihan, D.L.: MR diffusion tensor spectroscopy and imaging. Biophys. J. 66, 259–267 (1994)
8. Bassingthwaighte, J.B.: The Physiome Project: Why Now? and How? Proc. 34th International Congress of Physiological Sciences 2001
9. Beeler, G.W., Reuter, H.: Reconstruction of the action potential of ventricular myocardial fibres. J. Physiol. 268, 177–210 (1977)
10. Berenfeld, O., Abboud, S.: Simulation of cardiac activity and the ECG using a heart model with a reaction-diffusion action potential. Med. Eng. Phys. 18, 615–625 (1996)
11. Berenfeld, O., Jalife, J.: Purkinje-Muscle Reentry as a Mechanism of Polymorphic Ventricular Arrhythmias in a 3-Dimensional Model of the Ventricles. Circ. Res. 82, 1063–1077 (1998)
12. Bradley, C.P., Pullan, A.J., Hunter, P.J.: Geometric modelling of the human torso using cubic Hermite elements. Ann. Biomed. Eng. 25, 96–111 (1997)
13. Bradley, C.P.: The Computational Performance of a High-Order Coupled FEM/BEM Procedure in Electropotential Problems. Ph. D. thesis. The University of Auckland, New Zealand 1998
14. Buist, M., Sands, G., Hunter, P., Pullan, A.: A Deformable Finite Element Derived Finite Difference Method for Cardiac Activation Problems. Ann. Biomed. Eng.
15. Buist, M., Pullan, A.: Torso Coupling Techniques for the Forward Problem of Electrocardiology. Ann. Biomed. Eng. 30(10), 1299–1312 (2002)
16. Burger, H.C., van Milaan, J.B.: Heart-vector and leads.. Br. Heart J. 8, 157–61 (1946)
17. Cherry, E.M., Greenside, H.S., Henriquez, C.S.: A Space-Time Adaptive Method for Simulating Complex Cardiac Dynamics. Phys. Rev. Lett. 84(7), 1343–1346 (2000)
18. Cimponeriu, A., Starmer, C.F., Bezerianos, A.: A Theoretical Analysis of Acute Ischemia and Infarction Using ECG Reconstruction on a 2-D Model of Myocardium. IEEE Trans. Biomed. Eng. 48(1), 41–54 (2001)
19. Colli Franzone, P., Guerri, L., Pennacchio, M., Taccardi, B.: Spread of Excitation in 3-D Models of the Anisotropic Cardiac Tissue. II. Effects of Fiber Architecture and Ventricular Geometry. Math. Biosci. 147, 131–171 (1998)
20. Colli Franzone, P., Guerri, L., Pennacchio, M., Taccardi, B.: Spread of Excitation in 3-D Models of the Anisotropic Cardiac Tissue. III. Effects of ventricular Geometry and fiber structure on the potential distribution. Math. Biosci. 151, 51–98 (1998)
21. Cordier, F., Magnenat-Thalmann, N.: Comparison of Two Techniques for Organ Reconstruction Using Visible Human Dataset. Modeling for Medical Applications. Siggraph 2000
22. Dautray, R., Lions, J.-L.: Mathmatical Analysis and Numerical Methods for Science and Technology. Vol II: Functional and Variational Methods. Berlin, Heidelberg, New York: Springer 1988
23. Einthoven, W.: Die galvanometrische Registrierung des menschlichen Elektrokardiogramms, zugleich eine Beurteilung der Anwendung des Capillarelektrometers in der Physiologie. Pfluegers Arch. 99, 472–480 (1903)
24. FitzHugh, R.: Thresholds and plateaus in the Hodgkin-Huxley nerve equations. J. Gen. Physiol. 43, 867–896 (1960)
25. Frank, E.: Absolute quantitative comparison of instantaneous QRS equipotentials on a normal subject with dipole potentials on a homogeneous torso model. Circ. Res. 3, 243–51 (1955)
26. Frank, E.: An accurate, clinically practical system for spatial vectorcardiography. Circulation 13, 737–49 (1956)
27. Garrido, L., Wedeen, V.J., Kwong, K.K., Spencer, U.M. Kantor, H.L.: Anisotropy of water diffusion in the myocardium of the rat. Circ. Res. 74, 789–793 (1994)
28. Gear, C.W.: The Automatic Integration of Stiff Ordinary Differential Equations. Comm. of the ACM 14, 176–179 (1971)
29. Gelernter, H.L., Swihart, J.C.: A mathematical-physical model of the genesis of the electrocardiogram. Biophys. J. 4, 285–301 (1964)
30. Geselowitz, D.B.: Multipole representation for an equivalent cardiac generator. Proc. IRE 48, 75–79 (1960)
31. Geselowitz, D.B., Miller, W.T.: A bidomain model for anisotropic cardiac muscle. Ann. Biomed. Eng. 11, 191–206 (1983)
32. Geselowitz, D.B., Smith, S., Mowrey, K., Berbari, E.J.: Model Studies of Extracellular Electrograms Arising from an Excitation Wave Propagating in a Thin Layer. IEEE Trans. Biomed. Eng. 38(6), 526–531 (1991)
33. Goldberger, E.: A simple, indifferent, electrocardiographic electrode of zero potential and a technique of obtaining augmented, unipolar, extremity leads. Am. Heart J. 23, 483–492 (1942)
34. Green, L.S., Taccardi, B., Ershler, P.R., Lux, R.L.: Effects of Conducting Media on Isopotential and Isochrione Distributions. Circulation 84(6), 2513–2521 (1991)
35. Gulrajani, R.M.: Models of electrical activity of the heart and computer simulation of the electrocardiogram. Crit. Rev. Biomed. Eng. 16(1), 1–66 (1998)
36. Gulrajani, R.M., Trudel, M.C., Leon, L.J.: A Membrane-Based Computer Heart Model Employing Parallel Processing. Biomedizinische Technik 46, 20–22 (2001)
37. Gulrajani, R.M., Roberge, F.A., Mailloux, G.E.: The forward problem of electrocardiography/The inverse problem of electrocardiography. In: Macfarlane, P., Lawrie, T.V. (eds.): Comprehensive Electrocardiography. Permagon Press 1989
38. Harrild, D.M., Henriquez, C.S.: A Finite Volume Model of Cardiac Propagation. Ann. Biomed. Eng. 25, 315–334 (1997)
39. Harrild, D.M., Penland, C., Henriquez, C.S.: A Flexible Method for Simulating Cardiac Conduction in Three-Dimensional Complex Geometries. J. Electrocardiol. 33, 241–251 (2000)
40. Henriquez, C.S., Plonsey, R.: Effect of resistive discontinuities on waveshape and velocity in a single cardiac fibre. Med. Biol. Eng. Comput. 25, 428–438 (1987)
41. Henriquez, C.S.: An examination of a computationally efficient algorithm for modeling propagation in cardiac tissue. Innov. Tech. Biol. Med. 10, 26–35 (1989)
42. Henriquez, C.S., Trayanova, N., Plonsey, R.: A Planar Slab Bidomain Model for Cardiac Tissue. Ann. Biomed. Eng. 18, 367–376 (1990)
43. Henriquez, C.S.: Simulating the Electrical Behavior of Cardiac Tissue Using the Bidomain Model. Critical Reviews in Biomedical Engineering 21, 1–77 (1993)
44. Hodgkin, A.L., Huxley, A.F.: A quantitative description of membrane current and its application to conduction and excitation in nerve. J. Physiol. 117, 500–544 (1952)
45. Hogues, H., Leon, L.J., Roberge, F.A.: A Model Study of Electric Field Interactions Between Cardiac Myocytes. IEEE Trans. Biomed. Eng. 39(12), 1232–1242 (1992)
46. Hookings, A.G.: A Computer Model of the Electrical Activation of the Heart. Ph. D. thesis. The University of Auckland, New Zealand 1988
47. Hren, R., Nenonen, J., Horacek, B.M.: Simulated Epicardial Potential Maps During Paced Activation Reflect Myocardial Fibrous Structure. Ann. Biomed. Eng. 26, 1022–1035 (1998)
48. Hsu, E.W., Mori, S.: Analytical expressions for the NMR apparanet diffusion coefficients in an anisotropic system and a simplified method for determining fiber orientation. Mgn. Reson. Med. 34, 194–200 (1995)
49. Huiskamp, G.J.: Simulation of depolarization in a membrane-equations-based model of the anisotropic ventricle. IEEE Trans. Biomed. Eng. 45(7), 847–855 (1998)
50. Huang, Q., Eason, J.C., Claydon, F.J.: Membrane Polarization Induced in the Myocardium by Defibrillation Fields: An Idealized 3-D Finite Element Bidomain/Monodomain Torso Model. IEEE Trans. Biomed. Eng. 46(1), 370–373 (1999)
51. Hunter, P.J., McNaughton, P.A., Noble, D.: Analytical Models of Propagation in Excitable Cells. Prog. Biophys. Molec. Biol. 30, 99–144 (1975)
52. Hunter, P.J.: The IUPS Physiome Project: Progress and Plans Proc. 34th International Congress of Physiological Sciences 2001
53. Jafri, S., Rice, J., Winslow, R.: Cardiac Ca^{2+} dynamics: the role of ryanodine receptor adaptation and sarcoplasmic reticulum load. Biophys. J. 74, 1149–1168 (1998)
54. The joint European Society of Cardiology/American College of Cardiology Committee: Myocardial infarction redefined – a consensus document of The joint European Society of Cardiology/American College of Cardiology committee for the redefinition of myocardial infarction. J. Amer. Col. Cardiol. 36, 959–69 (2000)
55. Kauppinen, P., Hyttinen, J., Laarne, P., Malmivuo, J.: A software implementation for detailed volume conductor modelling in electrophysiology using finite difference method. Computer Methods and Programs in Biomedicine 58, 181–203 (1999)

56. Kossmann, C.E., Johnston, F.D.: The precordial electrocardiogram. I. The potential variations of the precordium and of the extremities in normal subjects. Am. Heart J. 10, 925–941 (1935)
57. Krassowska, W., Neu, J.C: Effective boundary condtions for syncytial tissues. IEEE Trans. Biomed. Eng. 41(2), 143–150 (1994)
58. Le Grice, I.J., Hunter, P.J., Smaill, B.H.: Laminar structure of the heart: a mathematical model. Am. J. Physiol. Heart. Circ. Physiol. 272, H2466–H2476 (1997)
59. Leon, L.J., Horacek, B.M.: Computer Model of Excitation and Recovery in the Anisotropic Myocardium. I: Rectangular and Cubic Arrays of Excitable Elements. J. Electrocardiol. 24, 1–14 (1991)
60. Leon, L.J., Horacek, B.M.: Computer Model of Excitation and Recovery in the Anisotropic Myocardium. II: Excitation in the Simplified Left Ventricle. J. Electrocardiol. 24, 17–31 (1991)
61. Leon, L.J., Horacek, B.M.: Computer Model of Excitation and Recovery in the Anisotropic Myocardium. III: Arrhythmogenic Conditions in the Simplified Left Ventricle. J. Electrocardiol. 24, 33–41 (1991)
62. Lesh, M.D., Pring, M., Spear, J.F.: Cellular uncoupling can unmask dispersion of action potential duration in ventricular myocardium, a computer modeling study. Circ. Res. 65, 1426–1440 (1989)
63. Lewis, T.: The mechanism and graphic registration of the heart beat. 3rd edn. London: Shaw & Sons Ltd. 1925
64. Lorensen, W., Cline, H.: Marching cubes: A high-resolution 3-D surface construction algorithm. Computer Graphics 21(3), 163–169 (1987)
65. Luo, C.H., Rudy, Y.: A Model of the Ventricular Cardiac Action Potential: Depolarisation, Repolarisation, and Their Interaction. Circ. Res. 68, 1501–1526 (1991)
66. Luo, C.H., Rudy, Y.: A dynamic model of the cardiac ventricular action potenial. Circ. Res. 74, 1071–1096 (1994)
67. MacLeod, R.S., Taccardi, B., Lux, R.L.: The Influence of Torso Inhomogeneities on Epicardial Potentials. Computers in Cardiology, 793–796 (1994)
68. McFee, R., Parungao, A.: An orthogonal lead system for clinical electrocardiography. Am. Heart J. 62, 93–100 (1961)
69. McFee, R., Rush, S.: Qualitative effects of thoracic resistivity variations on the interpretation of electrocardiograms: The Brody effect. Am. Heart J. 74, 642–651 (1967)
70. McFee, R., Rush, S.: Qualitative effects of thoracic resistivity variations on the interpretation of electrocardiograms: The low resistance surface layer. Am. Heart J. 74, 48–61 (1968)
71. Menown, I.B., Mackenzie, G., Adgey, A.A.: Optimizing the initial 12-lead electrocardiographic diagnosis of acute myocardial infarction. Eur. Heart J. 21, 275–83 (2000)
72. Miller, W.T., Geselowitz, D.B.: Simulation Studies of the Electrocardiogram I. The Normal Heart. Circ. Res. 43(2), 445–454 (1978)
73. Muller-Borer, B.J., Erdman, D.J., Buchanan, J.W.: Electrical Coupling and Impulse Propagation in Anatomically Modeled Ventricular Tissue. IEEE Trans. Biomed. Eng. 41(5), 445–454 (1994)
74. Muzikant, A.L., Henriquez, C.S.: Bipolar Stimulation of a Three-Dimensional Bidomain Incorporating Rotational Anisotropy. IEEE Trans. Biomed. Eng. 45(4), 449–462 (1998)
75. Nagumo, J., Animoto, S., Yoshizawa, S.: An Active Pulse Transmission Line Simulating Nerve Axon. Proc. Inst. Radio Engineers 50, 2061–207 (1962)
76. Nielsen, P.M.F., Le Grice, I.J., Smail, B.H., Hunter, P.J.: Mathematical model of geometry and fibrous structure of the heart. Am. J. Physiol. Heart. Circ. Physiol. 260, H1365–H1378 (1991)
77. DiFrancesco, D., Noble, D.: A model of the cardiac electrical activity incoportation ionic pumps and concentration changes. Philos. Trans. R. Soc. Lond. Biol. 307, 353–398 (1985)
78. Noble, D., Varghese, A., Kohl, P., Noble, P.: Improved guinea-pig ventricular cell model incorporating a diadic space, I_{Kr} and I_{Ks}, and length- and tension-dependent processes. Can. J. Cardiol. 14(1), 123–134 (1998)
79. Noble, D., Rudy, Y.: Models of cardiac ventricular action potentials: iterative interation between experiment and simulations. Philos. Trans. R. Soc. Lond. Biol. 359, 1127–1142 (2001)
80. Plonsey, R.: Bioelectric Phemomena. New York: McGraw Hill 1969
81. Plonsey, R., Barr, R.C.: Mathematical Modelling of Electrical Activity of the Heart. J. Electrocardiol. 20(3), 219–226 (1987)
82. Pollard, A.E., Hooke, N., Henriquez, C.S.: Cardiac propagation simulation. Crit. Rev. Biomed. Eng. 20, 171–210 (1992)
83. Porras, D., Rogers, J.M., Smith, W.M., Pollard, A.E.: Distributed computing for membrane-based modelling of action potential propagation. IEEE Trans. Biomed. Eng. 47(8), 1051–1057 (2000)
84. Qu, Z., Garfinkel, A.: An Advanced Algorithm for Solving Partial Differential Equation in Cardiac Conduction. IEEE Trans. Biomed. Eng. 46, 1166–1168 (1999)
85. Quan, W., Evans, S.J., Hastings, H.M.: Efficient Integration of a Realistic Two-Dimensional Cardiac Tissue Model by Domain Decompostion. IEEE Trans. Biomed. Eng. 45, 372–385 (1998)
86. Ramon, C., Wang, Y., Haueisen, J., Schimpf, P.: Effects of myocardial anisotropy on the torso current flow patterns, potentials and magnetic fields. Phys. Med. Biol. 45, 1141–1150 (2000)
87. Resse, T.G., Weisskoff, R.M., Smith, R.N., Rosen, B.R., Dinsmore, R.E., Wedeen, V.J.: Imaging myocardial fiber architecture in vivo with magnetic resonance. Magn. Reson. Med. 34, 786–791 (1995)
88. Rogers, J.M.: Finite Element Modeling of Cardiac Activation Dynamics. Ph. D. thesis. University of California, San Diego 1993
89. Rogers, J.M., McCulloch, A.D.: A Collocation-Galerkin Finite Element Model of Cardiac Action Potential Propagation. IEEE Trans. Biomed. Eng. 41(8), 743–757 (1994)
90. Rogers, J.M., McCulloch, A.D.: Nonuniform Muscle Fiber Orientation Causes Spiral Wave Drift in a Finite Element Model of Cardiac Action Potential Propagation. J. Cardiovasc. Electrophysiol. 5, 496–509 (1994)
91. Roth, B.J.: Electrical Conductivity Values Used with the Bidomain Model of Cardiac Tissue. IEEE Trans. Biomed. Eng. 44(4), 326–328 (1997)
92. Rudy, Y.: From Genome to Physiome: Integrative Models of Cardiac Excitation. Ann. Biomed. Eng. 28, 945–950 (2000)
93. Sachse, F.B., Werner, C.D., MeyerWaarden, K., Dössel, O.: Development of a human body model for numerical calculation of electrical fields. Comp. Med. Imag. Graph. 24(3), 165–171 (2000)
94. Saleheen, H.I., Ng, K.T.: A new three dimensional finite-differenc bidomain formulation for inhomogeneous anisotropic cardiac tissues. IEEE Trans. Biomed. Eng. 45(1), 15–25 (1998)
95. Salu, Y.: Implementing a consistency criterion in numerical solution of the bioelectric forward problem. IEEE Trans. Biomed. Eng. 27(6), 338–341 (1980)
96. Sands, G.B.: Mathematical Model of Ventricular Activation in an Anatomically Accurate Deforming Heart. Ph. D. thesis. The University of Auckland, New Zealand 1996
97. Schmidt, J.A., Pilkington, T.C.: The Volume Conductor Effects of Anisotropic Muscle on Body Surface Potentials Using an Eccentric Spheres Model. IEEE Trans. Biomed. Eng. 38(3), 300–303 (1991)
98. Schmitt, O.H.: Biological information processing using the concept of interpenetrating domain. In: Leibovic, K.N. (ed.): Information Processing in the Nervous System. Berlin, Heidelberg, New York: Springer 1969
99. Sederholm, M., Grøttum, P., Erhardt, L., Kjekshus, J.K.: Quantitative assessment of myocardial ischemia and necrosis by continuous vectorcardiography and measurement of creatine kinase release in patients. Circulation 68, 1006–12 (1983)
100. Shahidi, A.V., Savard, P., Nadeau, R.: Forward and Inverse Problems of Electrocariography: Modeling and Recovery of Epicardial Potentials in Humans. IEEE Trans. Biomed. Eng. 41(3), 249–256 (1994)
101. Shampine, L.F., Gordon, M.K.: Computer solution of ordinary differential equations: the initial value problem. Pub. by Freeman, W.H., 1975
102. Sicouri, S., Antzelevitch, C.: A Subpopulation of Cells With Unique Electrophysiological Properties in the Deep Subepicardium of the Canine Ventricle. Circ. Res. 68(6), 1729–1741 (1991)
103. Simson, M.B.: Use of signals in the terminal QRS complex to identify patients with ventricular tachycardia after myocardial infarction. Circulation 64, 235–42 (1981)
104. SippensGroenewegen, A., Hauer, R.N.W., van Hemel, N.M., Janse, M.J., de Medina, E.O.R.: Atlas of Paced Body Surface QRS Integral Maps for Localization of the Site Of Origin of Postinfarction Ventricular Tachycardia. J. Electrocardiol. 27(Suppl.), 105–112 (1994)
105. Skouibinea, K., Trayanova, N., Moore, P.: Anode/Cathode Make and Break Phenomena During Defibrillation: Does Electroporation Make a Difference? IEEE Trans. Biomed. Eng. 46, 769–777 (1999)
106. Skouibinea, K., Trayanova, N., Moore, P.: A numerically efficient model for simulation of defibrillation in an active bidomain sheet of myocardium. Math. Biosc. 166(1), 85–100 (2000)
107. Stanley, P.C., Pilkington, T.C., Morrow, M.N.: The Effects of Thoracic Inhomogeneities on the Relationship Between Epicardial and Torso Potentials. IEEE Trans. Biomed. Eng. 33(3), 273–284 (1986)

108. Stanley, P.C., Pilkington, T.C.: The combination method: A numerical technique for electrocardiographic calculations. IEEE Trans. Biomed. Eng. 36(4), 456–461 (1989)
109. Street, A.M., Plonsey, R.: Propagation in Cardiac Tissue Adjacent to Connective Tissue: Two-Dimensional Modeling Studies. IEEE Trans. Biomed. Eng. 46(1), 19–25 (1999)
110. Sundnes, J., Lines, G.T., Tveito, A.: Efficient solution of ordinary differential equations modeling electrical activity in cardiac cells. Math. Biosci. 172, 55–72 (2001)
111. Sundnes, J., Lines, G.T., Mardal, K.A., Tveito, A.: Multigrid block preconditioning for the coupled bidomain and forward problem. Accepted for publication in Computer Methods in Biomechanics and Biomedical Engineering
112. Taccardi, B.: Distribution of Heart Potentials on the Thoracic Surface of Normal Human Subjects. Circ. Res. 12, 341–352 (1963)
113. Thivierge, M., Gulrajani, R. Savard, P.: Effects of Rotational Myocardial Anisotropy in Forward Potential Computations with Equivalent Heart Dipoles. Ann. Biomed. Eng. 25, 477–498 (1997)
114. Tomlinson, K.A., Hunter, P.J., Pullan, A.J.: On the choice of a derivative boundary element formulation using Hermite interpolation. Int. J. Numer. Methods Eng. 39, 451–468 (1996)
115. Tomlinson, K.A.: Finite element solution of an eikonal equation for excitation wavefront propagation in ventricular myocardium. Ph. D. thesis. The University of Auckland, New Zealand 2000
116. Trayanova, N.A., Roth, B.J., Malden, L.J.: The response of a spherical heart to a uniform electric field: A bidomain analysis of cardiac stimulation. IEEE Trans. Biomed. Eng. 40, 899–908 (1993)
117. Trayanova, N.A.: Discrete Versus Syncytial Tissue Behaviour in a Model of Cardiac Stimulation – I: Mathematical Formulation. IEEE Trans. Biomed. Eng. 43(12), 1129–1140 (1996)
118. Trayanova, N.A.: Discrete Versus Syncytial Tissue Behaviour in a Model of Cardiac Stimulation – II: Results of Simulation. IEEE Trans. Biomed. Eng. 43(12), 1141–1150 (1996)
119. Trayanova, N.A., Bray, M.A.: Membrane Refractoriness and Excitation Induced in Cardiac Fibres by Monophasic and Biphasic Shocks. J. Cardiovasc. Electrophysiol. 8(7), (1997)
120. Tung, L.: A Bi-domain model for describing ischemic myocardial D-C potentials. Ph. D. thesis. MIT, Cambridge, MA 1978
121. van Capelle, F.J.L., Durrer, D.: Computer Simulation of Arrhythmias in a Network of Coupled Excitable Elements. Circ. Res. 47, 454–466 (1980)
122. The Visible Human Project, URL: http://www.nlm.nih.gov/research/visible/visible_human.html
123. Waller, A.D.: A demonstraion on man of electromotive changes accompanying the heart's beat. J. Physiol. 8, 229–234 (1887)
124. Waller, A.D.: Introductory address on the electromotive properties of the human heart. Br. Med. J. 2, 751–754 (1888)
125. Waller, A.D.: On the electromotive changes connected with the beat of the mammalian heart, and of the human heart in particular. Phil. Trans. R. Soc. London, Ser. B 180, 169–194 (1889)
126. Wei, D., Okazaki, O., Harumi, K., Harasawa, E., Hosaka, H.: Comparative simulation of excitation and body surface electrocardiogram with isotropic and anisotropic computer heart models. IEEE Trans. Biomed. Eng. 42(4), 343–357 (1995)
127. Weixue, L., Ling, X.: Computer simulation of epicardial potentials using a heart-torso model with realistic geometry. IEEE Trans. Biomed. Eng. 43(2), 211–217 (1996)
128. Wilson, F.N., MacLeod, A.G., Barker, P.S.: The Distribution of the Currents of Action and of Injury Diplayed by Heart Muscle and Other Excitable Tissues. Univeristy of Michigan Press, Ann Arbor: 1933
129. Wilson, F.N., Macleod, A.G., Barker, P.S., Johnston, F.D.: The determination and the significance of the areas of the ventricular deflections of the electrocardiogram. Am. Heart J. 10, 46–61 (1934)
130. Wilson, F.N., Bayley, R.H.: The electric field of an eccentric dipole in a homogeneous spherical conducting medium. Circulation 1, 84–92 (1950)
131. Winslow, R.L., Rice, J., Jafri, S., Marban, E., O'Rourke, B.: Mechanisms of altered excitation-contraction coupling in canine tachycardia-induced heart failure, II. Model studies. Circ. Res. 84, 571–586 (1999)
132. Winslow, R.L., Scollan, D.F., Holmes, A., Yung, C.K., Zhang, J., Jafri, M.S.: Electrophysiological modeling of cardiac ventricular function: From cell to organ. Ann. Rev. Biomded. Eng. 2, 119–155 (2000)